

Shear-induced breaking of large internal solitary waves

DORIAN FRUCTUS¹, MAGDA CARR², JOHN GRUE^{1†},
ATLE JENSEN¹ AND PETER A. DAVIES³

¹Mechanics Division, Department of Mathematics, University of Oslo, PO Box 1053, Blindern, 0316 Oslo, Norway

²School of Mathematics and Statistics, University of St Andrews, Fife KY16 9SS, UK.

³Department of Civil Engineering, The University, Dundee DD1 4HN, UK.

(Received 14 January 2008 and in revised form 7 November 2008)

The stability properties of 24 experimentally generated internal solitary waves (ISWs) of extremely large amplitude, all with minimum Richardson number less than $1/4$, are investigated. The study is supplemented by fully nonlinear calculations in a three-layer fluid. The waves move along a linearly stratified pycnocline (depth h_2) sandwiched between a thin upper layer (depth h_1) and a deep lower layer (depth h_3), both homogeneous. In particular, the wave-induced velocity profile through the pycnocline is measured by particle image velocimetry (PIV) and obtained in computation. Breaking ISWs were found to have amplitudes (a_1) in the range $a_1 > 2.24\sqrt{h_1 h_2}(1 + h_2/h_1)$, while stable waves were on or below this limit. Breaking ISWs were investigated for $0.27 < h_2/h_1 < 1$ and $4.14 < h_3/(h_1 + h_2) < 7.14$ and stable waves for $0.36 < h_2/h_1 < 3.67$ and $3.22 < h_3/(h_1 + h_2) < 7.25$. Kelvin–Helmholtz-like billows were observed in the breaking cases. They had a length of $7.9h_2$ and a propagation speed 0.09 times the wave speed. These measured values compared well with predicted values from a stability analysis, assuming steady shear flow with $U(z)$ and $\rho(z)$ taken at the wave maximum ($U(z)$ horizontal velocity profile, $\rho(z)$ density along the vertical z). Only unstable modes in waves of sufficient strength have the chance to grow sufficiently fast to develop breaking: the waves that broke had an estimated growth (of unstable modes) more than 3.3–3.7 times than in the strongest stable case. Evaluation of the minimum Richardson number (Ri_{min} , in the pycnocline), the horizontal length of a pocket of possible instability, with wave-induced $Ri < 14$, (L_x) and the wavelength (λ), showed that all measurements fall within the range $Ri_{min} = -0.23L_x/\lambda + 0.298 \pm 0.016$ in the $(L_x/\lambda, Ri_{min})$ -plane. Breaking ISWs were found for $L_x/\lambda > 0.86$ and stable waves for $L_x/\lambda < 0.86$. The results show a sort of threshold-like behaviour in terms of L_x/λ . The results demonstrate that the breaking threshold of $L_x/\lambda = 0.86$ was sharper than one based on a minimum Richardson number and reveal that the Richardson number was found to become almost antisymmetric across relatively thick pycnoclines, with the minimum occurring towards the top part of the pycnocline.

1. Introduction

Internal solitary waves (ISWs) occur in all of the world's oceans. The waves are generated by tidal flows across subsea ridges or continental shelves or by the relaxation

† Email address for correspondence: johng@math.uio.no

of pools of light or heavy water masses trapped by the wind along complex coastal topographies. The waves are typically nonlinear and pulse-shaped and may attain very large amplitudes compared with the water depth. Recent reviews (in particular, Ostrovsky & Stepanyants 2005; Helfrich & Melville 2006; Grue 2006) give the status of research on nonlinear ISWs. Very-large-amplitude waves may be stable, or they may overturn and break because of either convective or shear-driven instability (or a combination of both). The stability of ISWs is under current investigation because of the fundamental role played by the waves in determining aspects of local and global flow processes in the ocean. In particular, breaking ISWs enhance ambient turbulent motions, contribute to overall mixing and redistribute the potential energy in the water column. Moreover, the breaking caused by ISWs has strong implications for the distributions of certain biological and geological tracers in the ocean.

ISWs may become highly nonlinear and, at the same time, remain stable (non-breaking), as exemplified by the very large, stable ISWs observed in the Coastal Ocean Probing Experiment (COPE) on the northern Oregon continental shelf. Wave amplitudes up to 4–5 times the thickness of the mixed upper layer at rest were documented by Stanton & Ostrovsky (1998) and reproduced by theoretical models by Ostrovsky & Grue (2003). Another very large wave, also stable, was measured in the South China Sea and documented by Duda *et al.* (2004; see also figure 2(b) in Helfrich & Melville 2006). The wave had a vertical excursion of the mixed upper layer of 150 m from the level at rest of 40 m, giving a non-dimensional amplitude of 3.75 relative to the thickness of the mixed upper layer, in a total water depth of 340 m. In the present investigation, large, stable ISWs with a relative amplitude corresponding to the COPE waves have been studied in a series of laboratory experiments. Two specific examples (runs 16 and 20 in table 1) are highlighted in which the waves have maximal excursions (amplitudes) of the mixed upper layer of 3.2 and 4.5 times the thickness at rest, respectively (see §4). In addition, stable ISWs of even larger relative amplitudes have been generated in the laboratory, including a case in which the excursion of the isopycnal surface separating the mixed upper layer from the pycnocline was as large as 8.6 times the undisturbed thickness of the mixed layer itself. The relative amplitude of this (stable) wave (see run 24, table 1, and figure 3c) was about twice as large as the ISWs measured in COPE.

Shear instability plays a fundamental role in internal wave breaking and is investigated in the present paper. For a parallel stratified shear flow, Miles (1961) and Howard (1961) proved that $g\beta - (1/4)U'^2 > 0$ is a sufficient condition for stability, where $g\beta$ is the Brunt–Väisälä frequency squared and U' is the vertical shear in the horizontal velocity. Moreover, Miles (1961) pointed out that the kinetic energy of a normal mode in an ideal fluid may be infinite if the (non-negative) Richardson number (Ri) drops below 1/4. Scotti & Corcos (1972) investigated experimentally the instability of parallel stratified shear flow, and Hazel (1972) developed two computer programs to integrate the Taylor–Goldstein (T-G) equation numerically for a set of velocity profiles, finding that a steady shear flow became unstable when Ri was lower than 0.2. Hazel (1972) expressed in his conclusion that Miles’s necessary condition for instability is quite a good *ad hoc* sufficient criterion to use in the field. Recently, many works have been published on the Kelvin–Helmholtz (KH) instability in stratified shear layers, including, e.g. Caulfield & Peltier (2000), Peltier & Caulfield (2000), Staquet (2000) and Smyth, Nash & Moum (2005). The hydrodynamic instability of flows having a pycnocline comparatively much thinner than the shear layer were first examined by Holmboe (1962), who showed that KH instability occurs at small Ri , while at higher Ri , a second mode of instability occurs, consisting of two trains of

interfacial waves travelling at the same speed but in opposite directions with respect to the mean flow. Recent works on the Holmboe instability include Zhu & Lawrence (2001) and Carpenter, Lawrence & Smyth (2007). Alexakis (2005) has found that the shear layer must be twice as thick as the pycnocline for Holmboe instability to develop. In the present experiments, the wave-induced velocity shear layer and pycnocline are equally thick. Possible breaking because of a Holmboe instability is excluded.

The mixing associated with an ISW of small amplitude and having an interface assumed to be much thinner than the upper layer, which again was much thinner than the lower layer, was investigated by Bogucki & Garrett (1993). Expressing the wave speed c in terms of weakly nonlinear Korteweg–de Vries (KdV) and Benjamin–Ono (BO) theories, they expressed the Richardson number by $Ri = h_2 h_1 / a_1^2$, an asymptotic result when $a_1 / h_1 \rightarrow 0$. Here h_1 is the upper mixed layer thickness, h_2 the pycnocline thickness and a_1 the wave amplitude. Assuming occurrence of wave breaking for $Ri = 1/4$ they obtained a relation for the critical amplitude, namely $a_c = 2\sqrt{h_1 h_2}$. Breaking ISWs propagating shoreward on Oregon’s continental shelf (measured by Moum *et al.* 2003) had values of Richardson number that could be estimated from observation to be larger than $1/4$. Breaking progressive interfacial waves were recently investigated in the laboratory by Troy & Koseff (2005), who suggested that the time scale of the destabilizing shear imposes an additional constraint on the (shear) instability that lowers the critical Richardson number in their periodic waves below $1/4$. The wave breaking occurred at a critical wave steepness that depended on the wavelength. By large eddy simulations (LESs) for the motion on laboratory scale, Fringer & Street (2003) studied how incipient two-dimensional instability develops into a three-dimensional convective pattern for a pycnocline of sufficiently finite thickness. The critical Richardson number at breaking was around $Ri_{min} = 0.13$ in their study.

In contrast to the situation obtained with the above periodic internal waves, experimental study of the stability of large-amplitude ISWs have not yet been published. Estimates of the minimal values of Ri in large-amplitude, laboratory-generated ISWs that are either stable or unstable with respect to shear are presented here. In the cases reported in this paper, the undisturbed background stratification consists of a three-layer system in which two homogeneous layers are separated by a linearly stratified pycnocline. (In a complementary paper by Carr *et al.*, 2008, waves in a two-layer system are measured for cases in which the upper layer is linearly stratified and the lower layer homogeneous.) The density is continuous in all of the experiments. The experimental velocity field, particularly the velocity profile through the pycnocline, is measured using particle image velocimetry (PIV). The experiments are complemented by fully nonlinear computations of ideal non-breaking ISWs that move with constant speed and shape. The observed features of the non-breaking experimental waves compare well with the computations; for cases in which there is evidence of breaking in the trailing part of the wave, the computations still describe well the structure of the leading non-breaking portion. The theory is used to evaluate precisely the wave-induced density field (of the non-breaking part of the waves). By fitting the computational velocity fields to their measured laboratory counterparts, the local value of the Richardson number is obtained by computation. For non-breaking waves, the difference between computation and experiment is very small. For breaking waves the difference between computation and measurement is used to obtain precise streamlines of the billows that are induced by the shear instability, in the trailing part of the wave. A stability analysis is also presented; and the T-G equation with the

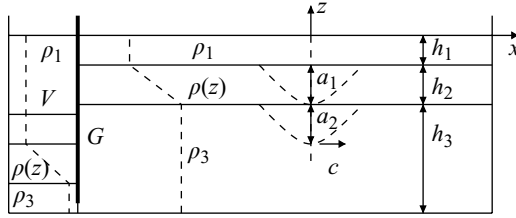


FIGURE 1. Schematic diagram of experimental arrangement. Tank dimensions and typical density profile described in §2.1. Layer depths and amplitudes given in table 1.

velocity and density profiles obtained at the maximum of the computational wave is solved. The predicted wavenumber and wave speed of the instability fits well with the experimental measurement. Finally, a new stability criterion for shear instability of ISWs is derived, which takes into account the horizontal extent of the domain of the wave within which $Ri < 1/4$, in addition to the minimal value of the Richardson number. The new stability criterion is consistent with all observations.

The paper is organized as follows: the next section presents the experimental set-up and procedures for wave generation and measurement. Section 3 describes the nonlinear computation of the waves and gives an exact formula for the calculation of the Richardson number. In §4 the stability of waves and observation of KH billows are discussed. Stability calculations solving the T-G equation are performed. Finally, results are compared to other publications. In §5 the horizontal length (L_x) and shape of a pocket in which $Ri < 1/4$ (a pocket of possible instability) is computed for all experimental waves, as well as the wavelength (λ). A separation between stable and breaking waves is found at $L_x/\lambda = 0.86$. Accuracy is assessed in §5.2 and the effect of the Reynolds number in §5.3. Section 6 provides a summary and conclusion.

2. Experimental set-up and procedure

2.1. Wave tank facilities and wave generation

The experiments were performed in two different wave tank facilities having (length, width, depth) dimensions of (12.6 m \times 0.5 m \times 1 m) and (6.4 m \times 0.4 m \times 0.6 m), respectively. In all experiments, the lower layer was filled with a prepared solution of brine of prescribed density ρ_3 . The midlayer was then added carefully via a floating sponge arrangement. The double-bucket technique was used to obtain a linearly stratified midlayer with density ranging from ρ_3 to ρ_1 , and the top layer was then filled with a prepared solution of density ρ_1 . The top layer had thickness h_1 and bottom layer thickness h_3 , with pycnocline thickness h_2 (see figure 1). The Brunt-Väisälä frequency in the pycnocline was constant (at rest) and given by $N_\infty^2 = g\Delta(\rho_3 - \rho_1)/h_2\rho_3$, where $(\rho_3 - \rho_1)/\rho_3 \ll 1$. In all experiments, the relative density difference was approximately 2%.

Solitary waves of very large amplitude were generated by the step-pool technique (Grue *et al.* 1999), in which a gate was introduced after the layers had been filled, and a prescribed volume of brine of density ρ_1 was added behind the gate (see figure 1). By a careful choice of the initial volume, very-large-amplitude ISWs could be generated. By quickly removing the gate, a single solitary wave of depression was generated and propagated into the main section of the tank. The top of the fluid layer was in all experiments covered by plates of polystyrene. Note that with a large initial volume, a train of rank-ordered solitary waves may be expected to

develop, according to inverse scattering theory, assuming weak nonlinearity and use of the KdV equation, as investigated experimentally by Kao, Pan & Renouard (1985). However, the experimental generation of very large ISWs falls outside the range of the weakly nonlinear KdV theory. The generation of the large waves may be arranged such that nearly all of the volume trapped behind the gate goes into the volume of one single solitary wave. Generation, in this case, is very fast, with the leading front of the wave almost instantly taking the form of a theoretical solitary wave of very large amplitude. Examples are documented in Grue *et al.* (1999) and Sveen *et al.* (2002).

The ISWs moving along the pycnocline were characterized by their propagation speed c and amplitude. In this regard, it has been convenient to define two amplitudes of the waves, viz. the amplitude a_1 representing the maximal excursion of the mixed upper layer and the amplitude a_2 defining the maximal (negative) excursion of the lower layer (see figure 1). The two amplitudes are always similar (see table 1). For reference purposes, a coordinate system (x, z) is introduced, where x is the (horizontal) propagation direction of the wave and z is oriented vertically upward. The origin is chosen so that $x=0$ and $z=0$ correspond to the trough of the wave and the localized top of the water column. The point $x=0$ is moving with the (steady) wave.

2.2. Evaluation of wave speed in experiment

All the experimental waves considered here exhibited either no instability or shear instability developing at the trough of the waves. Using the streamline plots from the experiments, the exact spatial location of the wave core could be determined. The core was tracked during the passage of the wave to enable the propagation velocity c_{exp} to be evaluated in the experiment. The relative error in extracting c_{exp} in all experiments was estimated to be 8% at maximum, while the relative error in measuring the amplitude a_{exp} was estimated to be 2%.

Measured wave-propagation velocities were in the range 7–14 cm s⁻¹ in the small tank (e.g. 14 cm s⁻¹ in run 1; figure 3*d*) and 18–22 cm s⁻¹ in the large tank (e.g. 22 cm s⁻¹ in run 13; figure 3*a*). The complementary fully nonlinear wave speed and amplitude were always evaluated from the model (§3).

Wave amplitude reduction for waves similar to those studied here has been documented by Sveen *et al.* (2002) using the same wave tanks as in the present study, resulting in finding a typical frictional attenuation of about 1.3% and 4.8% per meter of propagation, in the large and small tanks, respectively. The wave amplitudes presented in table 1 correspond to the ones recorded in the field of view. Since the wave amplitude exhibits a small reduction during the propagation along the tank, the ratio L_x/λ (see §5 for definition of lengths L_x and λ) exhibits a small reduction, while Ri_{min} increases slightly. A wave that marginally breaks right after generation will then become stable after a while – typically after it is reflected from the wall in the far end. The reflected waves were not measured, however.

2.3. Particle image velocimetry

Particle image velocimetry (PIV) was used to visualize and quantify the experimental wave-induced velocity field in a vertical, two-dimensional, illuminated slice of the flow field. In the small tank, a continuous, collimated light sheet from an array of light boxes placed below the (transparent) base of the tank was used. The light sheet had a thickness of approximately 10 mm, and it illuminated a section of the tank 1.4 m wide and 0.6 m deep. The illuminated section was seeded with neutrally buoyant, light-reflecting tracer particles of ‘Pliolite’, having diameters in the range 150–300 μm. Motions within the vertical light sheet were viewed and recorded from the side, using a fixed digital video camera set-up outside the tank. The camera had

Ref.		Experimental results									Gardner	Fully nonlinear				Stability analysis				Observation	
run	date	h_1 cm	h_2 cm	h_3 cm	$\frac{h_2}{h_1}$	$\frac{h_3}{h_1+h_2}$	N s^{-1}	$\frac{a_1}{h_1+h_2}$	$\frac{a_2}{a_1}$	$\frac{c_{exp}}{c_0}$	$\frac{c_G}{c_0}$	$\frac{c}{c_0}$	R_{min}	$\frac{L_x}{\lambda}$	$\frac{2\pi a_1}{\lambda}$	$\frac{2\pi h_2}{\lambda}$	$\frac{\lambda_i}{h_2}$	c_r/c_0	$\gamma^{\frac{h_1+h_2}{c_0}}$		F
1	130605	5	2	30	0.4	4.29	3.46	1.59 ± 0.04	1.01 ± 0.05	1.47 ± 0.12	1.35	1.38	0.112	0.86	0.65	0.119	7.6	0.13	0.56	2.7	Breaking
2	190406	5	2	30	0.4	4.29	1.73	1.71 ± 0.04	1.01 ± 0.05	1.40 ± 0.11	1.36	1.40	0.103	0.91	0.83	0.140	8.3	0.13	0.60	2.8	Breaking
3	200605	5	2	29	0.4	4.14	3.43	1.42 ± 0.03	1.11 ± 0.05	1.35 ± 0.11	1.33	1.37	0.105	0.90	0.80	0.161	7.3	0.07	0.88	4.3	Breaking
4	180406	5	2	29	0.4	4.14	1.75	1.50 ± 0.04	1.06 ± 0.05	1.35 ± 0.11	1.33	1.37	0.100	0.90	0.67	0.128	7.7	0.09	0.73	3.6	Breaking
5	080206	11	4	64	0.36	4.27	2.32	1.54 ± 0.04	1.00 ± 0.05	1.41 ± 0.11	1.33	1.35	0.098	0.88	0.67	0.116	7.6	0.09	0.64	3.3	Breaking
6	080606	11	3	64	0.27	4.57	2.81	1.39 ± 0.03	1.00 ± 0.05	1.41 ± 0.11	1.30	1.35	0.082	0.91	0.77	0.119	6.8	0.13	0.93	4.3	Breaking
7	140606	9	3	64	0.33	5.33	2.65	1.61 ± 0.04	1.01 ± 0.05	1.41 ± 0.11	1.39	1.43	0.092	0.87	0.83	0.128	8.2	0.18	0.67	2.8	Breaking
8	130606	9	3	64	0.33	5.33	2.66	1.76 ± 0.04	1.01 ± 0.05	1.48 ± 0.12	1.39	1.45	0.083	0.94	0.85	0.120	8.2	0.14	0.79	3.7	Breaking
9	180705	2	2	28	1	7.00	3.32	2.36 ± 0.05	1.03 ± 0.05	1.68 ± 0.13	1.58	1.72	0.096	0.88	1.11	0.236	7.8	0.34	0.44	1.9	Breaking
10	190705	2	2	29	1	7.14	3.35	2.68 ± 0.06	1.01 ± 0.05	1.69 ± 0.14	1.63	1.73	0.087	0.94	1.21	0.226	7.7	0.30	0.50	2.3	Breaking
11	070606	5	5	67	1	6.70	1.96	2.54 ± 0.06	1.00 ± 0.05	1.82 ± 0.15	1.58	1.69	0.086	0.99	0.99	0.195	8.2	0.16	0.59	3.1	Breaking
12	070206	11	4	61	0.36	4.07	2.30	1.36 ± 0.03	1.01 ± 0.05	1.32 ± 0.11	1.32	1.34	0.12	0.78	0.67	0.132	7.5	0.08	0.39	1.5	Stable
13	090206	11	4	61	0.36	4.07	2.30	1.36 ± 0.03	1.00 ± 0.04	1.36 ± 0.11	1.32	1.34	0.12	0.78	0.67	0.132	7.5	0.08	0.39	1.5	Stable
14	200406	5	3	29	0.6	3.63	1.47	1.35 ± 0.03	1.02 ± 0.05	1.32 ± 0.11	1.34	1.36	0.17	0.62	0.72	0.20	6.8	0.20	0.19	0.6	Stable
15	080506	2	2	29	1	7.25	3.18	1.52 ± 0.03	1.10 ± 0.05	1.68 ± 0.13	1.62	1.60	0.23	0.37	1.05	0.34	∞	0	0	0	Stable
16	310106	5	10	57	2	3.80	1.46	1.06 ± 0.02	1.09 ± 0.05	1.44 ± 0.12	1.48	1.46	0.23	0.24	0.74	0.46	∞	0	0	0	Stable
17	010206	5	10	57	2	3.80	1.46	1.06 ± 0.02	1.09 ± 0.05	1.39 ± 0.11	1.48	1.46	0.23	0.24	0.74	0.46	∞	0	0	0	Stable
18	020206	5	10	58	2	3.87	1.43	1.21 ± 0.03	1.00 ± 0.04	1.41 ± 0.11	1.49	1.48	0.18	0.47	0.79	0.44	∞	0	0	0	Stable
19	010705	3	6	29	2	3.22	1.43	1.24 ± 0.03	1.02 ± 0.05	1.42 ± 0.11	1.44	1.42	0.15	0.67	0.69	0.37	7.1	0.37	0.04	0.1	Stable
20	030206	5	10	59	2	3.93	1.45	1.50 ± 0.03	1.01 ± 0.05	1.50 ± 0.12	1.50	1.50	0.13	0.75	0.79	0.35	7.8	0.37	0.14	0.6	Stable
21	060605	2	5	29	2.5	4.14	1.50	1.47 ± 0.03	1.06 ± 0.05	1.60 ± 0.13	1.56	1.57	0.15	0.56	0.94	0.46	8.2	0.63	0.02	0.1	Stable
22	060406	2	6	29	3	3.63	1.53	1.14 ± 0.03	1.08 ± 0.05	1.43 ± 0.11	1.53	1.52	0.15	0.56	0.79	0.52	∞	0	0	0	Stable
23	030406	2	6	28	3	3.50	1.47	1.56 ± 0.04	1.03 ± 0.05	1.55 ± 0.12	1.53	1.55	0.11	0.74	0.93	0.45	7.5	0.53	0.11	0.4	Stable
24	020605	1.5	5.5	29.5	3.67	4.14	1.47	1.74 ± 0.03	1.03 ± 0.05	1.67 ± 0.13	1.59	1.65	0.087	0.86	0.93	0.45	7.4	0.47	0.16	0.7	Stable

TABLE 1. Experimental parameters and predicted values from (i) extended KdV theory (Gardner *et al.* 1967), (ii) the fully nonlinear theory described in §3.2 and in the Appendix and (iii) the stability analysis from §7.1. $F = (\gamma L_x/2)/(|c - c_r|)$.

a spatial resolution and capture rate of 1372×1372 pixels and 24 frames per second respectively. In the large tank a 100 Hz, 15 mJ per pulse Nd:YAG laser illuminated a section approximately 0.5 m long, 2 mm thick and 1.0 m deep. The Pliolite tracer particles had diameters in the range 500 – 700 μm , and the camera had a spatial resolution of 1024×1024 pixels.

The dynamics of interest occurred mainly in the pycnocline and top layer. The cameras were positioned level with the surface of the undisturbed flow to avoid distortion and perspective errors in the upper portion of the flow field. The resulting video record of the flow within the illuminated window was processed using the software package DigiFlow (Dalziel 2006) to generate continuous, synoptic velocity field data throughout the water column. In all cases, the recording system was stationary with respect to the tank, and the ISW travelled through the illuminated measurement window.

In the small tank, the experimental field of view, 0.75 m wide and 0.345 m high, was centred about 4.14 m from the location of the gate at which the waves were generated. In pixels, the field of view was 1095 wide and 504 high; i.e. 1 pixel represented 0.68 mm in width and height. In the large tank the experimental field of view was 0.36 m by 0.36 m and 1024×1024 in pixels; i.e. 1 pixel represented 0.35 mm in width and height. The camera was positioned at 7.5 m from the end of the tank in which the wave was generated.

Sixty-five different experimental runs were performed using the three-layer configuration. Data from twenty-four of the experiments with the largest amplitude have been retained and presented here. The parameter values and observational data are presented in the first section of table 1. In the present experiments, $h_3/(h_1 + h_2)$ is in the range 3.2–7.3, h_2/h_1 in the range 0.27–3.67 and amplitude $a_1/(h_1 + h_2)$ in the range 1.06–2.68, while a_1/a_2 is always close to 1.

The breaking waves typically took the form of KH-like billows, starting at the trough of the wave within the pycnocline. Note that there are significant differences between this type of behaviour and the observations of convective breaking and instability (starting in the top layer of the flow) for cases in which the stable stratification comprises of a linearly stratified top layer above a lower homogeneous layer of brine (Carr *et al.* 2008).

2.3.1. Refractive index matching

Refractive index matching was accounted for in all runs by using a linear mapping transformation between measured world coordinates and images of the flow, implemented automatically by DigiFlow. The maximum variation over 100 mm in pixels between layers of different densities was found to be 1, in both tanks. One pixel approximated as 1 mm in the large tank and 0.68 mm in the small one, which gives a maximum variation due to refraction of 1 %.

3. Nonlinear computation of stable waves

3.1. Theoretical reference velocity; linear long-wave speed

The linear long-wave speed c_0 of the internal wave motion is a natural reference velocity for the experimental velocity field induced by the nonlinear motion and is determined by $c_0 = N_\infty h_2 / Y$ when $(\rho_3 - \rho_1) / \rho_3 \ll 1$ and Y is a function of h_1/h_2 and h_3/h_2 . The resulting non-dimensional velocity field then becomes independent of the relative density jump when this jump is small (as in the ocean, which is the case here) and is a function of h_1/h_2 , h_3/h_2 and the non-dimensional wave amplitude. For linear

waves, the stream function reads $\psi(x, z) = a_0 \phi(z) \exp(ikx)$, where a_0 denotes amplitude and $\phi(z)$ satisfies the T-G equation, $(d^2/dz^2 + N^2/c_{lin}^2 - k^2)\phi = 0$, with boundary conditions $\phi(z=0) = \phi(z = -h_1 - h_2 - h_3) = 0$ and with ϕ and $d\phi/dz$ continuous at the interfaces. In each layer N takes the value. Solution of the T-G equation takes the form $A_j \cos(\widehat{K}_j z) + B_j \sin(\widehat{K}_j z)$, where $\widehat{K}_j = \sqrt{N_j^2/c_{lin}^2 - k^2}$ and A_j and B_j are constants ($j = 1, 2, 3$), in each layer. The dispersion relation $c_{lin}(k)$ is obtained using the boundary conditions at $z=0$, $z = -h_1$, $z = -h_1 - h_2$, $z = -h_1 - h_2 - h_3$, giving $\widehat{K}_2^2 - T_1 T_2 - T_2 T_3 - T_3 T_1 = 0$, where $T_j = \widehat{K}_j \cot(\widehat{K}_j h_j)$. The linear long wave speed (c_0) is obtained by letting $k \rightarrow 0$ in the analysis. In the special case when $N_1 = N_3 = 0$ we obtain

$$\cot Y + \frac{h_2/(h_3 Y) - Y h_1/h_2}{1 + h_1/h_3} = 0. \quad (3.1)$$

The longest wave mode is obtained for $Y = N_\infty h_2/c_0$ in the interval $(0, \pi)$.

3.2. Computation of the nonlinear experimental ISWs

The experimental waves are recomputed using an integral equation method, in a frame of reference moving with the wave speed c , and thus are stationary. The fully nonlinear method solves the field equation in each of the layers, assuming that the Brunt–Väisälä frequency of the stratification at rest is constant in each layer. Relevant to the present experiments, where the density is constant in the upper and lower layers, the field equation in these layers reduces to the Laplace equation. In the midlayer in which the Brunt–Väisälä frequency at rest is constant and equal to N_∞ , the field equation becomes the Helmholtz equation. The fully nonlinear integral equation method used here was derived by Fructus & Grue (2004) and is described in more detail in the Appendix. A particular feature of the method is that it assumes a stepwise constant Brunt–Väisälä frequency at rest, which is ideal for the experimental stratifications under investigation. The method differs from the classical procedures derived by Tung, Chan & Kubota (1982) and Turkington, Eydeland & Wang (1991), assuming a continuously differentiable density profile in the vertical direction.

The experimental data and the computational predictions are compared in a stepwise procedure: firstly, the amplitude a_2 is estimated from the experiment, and, secondly, the stream function and the velocity field are computed. Thirdly, the local difference between the experimental and theoretical velocity vectors is computed. The procedure is iterated until the difference between theory and experiment is acceptably very small. The iterative procedure is used to identify the point of zero velocity in the experimental wave, with respect to both the vertical and horizontal components. The amplitudes a_1 and a_2 of the experimental waves (the maximal excursions of the upper and lower parts of the pycnocline), together with the wave speed, are obtained from the corresponding theoretical wave. The location of the pycnocline and its boundaries are obtained from the isolines of the theory and the experimental velocity maps.

3.3. Evaluation of the local Richardson number

The wave-induced velocity field was obtained in the experiments through PIV, thereby enabling the evaluation of the local shear, which is an essential component in the determination of the local Richardson number, Ri . The wave-induced change in the density field represents another important component in the understanding of the stability of the wave. The local density field can be evaluated from the theoretical computations of the wave, as in this case. The value of Ri is computed within the

pycnocline of the computational wave, using

$$Ri = \frac{\widehat{N}^2}{\omega^2} = \frac{c(c-u)}{\delta^2 N_\infty^2}. \quad (3.2)$$

The expression (3.2) is an exact result derived by Fructus & Grue (2004), their equation (5.2), and is valid when N_∞ differs from zero. In (3.2), \widehat{N} denotes the local Brunt–Väisälä frequency, ω the local vorticity, c the wave speed, u the horizontal velocity, δ the vertical excursion of the streamline relative to rest (defined in a frame of reference in which the wave is steady) and N_∞ the Brunt–Väisälä frequency at rest. It is noted that to derive (3.2), the local Brunt–Väisälä frequency (in the wave) is related to the quantity at rest (in the far field) by $\widehat{N} = N_\infty \sqrt{1 - u/c}$. Further, the vorticity, ω , induced by the wave motion, is obtained from the equation of motion, giving $\omega = \widehat{N}^2 \delta / (c - u) = N_\infty^2 \delta / c$.

As demonstrated below, there is only a very minor difference between the experimental and computational velocity fields, in the cases in which the waves are non-breaking. Further, in cases in which the waves break, the breaking takes place in the tail of the wave. There is good correspondence between experiment and theory in the leading part of the wave, even up to the point of maximum excursion. The computational estimate of Ri is thus very close to the local Ri in the non-breaking part in experiment. The value of Ri is obtained using (3.2), where c/c_0 , u/c and $\delta/(h_1 + h_2)$ are computed by the nonlinear code and $N_\infty h_2/c_0$ from (3.1). (The density field $\rho(x, z)$ is evaluated in the calculation.) Measurement of c and u/c compares favourably to computation (table 1 and figure 5). Discussion of the accuracy is given in §5.2 below.

Simulations were performed for all runs with 128, 256 and 512 nodes (resolution of the distributions σ_1 , σ_2 , $\widehat{\sigma}_2$, σ_3 and elevations η and $\widehat{\eta}$ in (A6)–(A8)) in order to ensure proper convergence. Convergence is generally slower in cases with very thin upper layer and very large amplitude, as in the most extreme case, run 24. The simulations with 512 nodes and layers h_1 , h_2 and h_3 of 1.5 cm, 5.5 cm and 29.5 cm exhibit good convergence.

3.4. Comparison with the Gardner equation

Using an approximate model, Stanton & Ostrovsky (1998) found that the extended KdV theory (eKdV) provided results in relatively good agreement with their observations of the very large ISWs in COPE. The eKdV equation – also termed the Gardner equation – reads

$$\frac{\partial \eta_G}{\partial \tau} + (c_{0G} + \alpha \eta_G + \alpha_1 \eta_G^2) \frac{\partial \eta_G}{\partial x} + \beta \frac{\partial^3 \eta_G}{\partial x^3} = 0, \quad (3.3)$$

where the coefficients are given in Stanton & Ostrovsky (1998). This equation is fully integrable and admits solitary wave solutions. The waves have a maximum wave speed and amplitude given by $c_{Gmax} = c_{0G} - \alpha^2/6\alpha_1$ and $a_{Gmax} = |\alpha/\alpha_1|$, respectively. Values of c_{Gmax} were obtained from (3.3), where the density distribution was approximated by a two-layer system with upper layer of thickness $h_1 + h_2/2$ and density ρ_1 and lower layer of thickness $h_3 + h_2/2$ and density ρ_3 . The estimates of c_{Gmax} are in rather good agreement with the observations and the fully nonlinear theory (see table 1). It is noted, however, that the amplitudes in the present experiments become larger than the limiting amplitude of the eKdV solution. While the fully nonlinear model is relevant for any of the experimental, non-breaking waves studied here, (3.3) is less useful in predicting the wave shapes and velocities of the measurements in such large-amplitude cases.

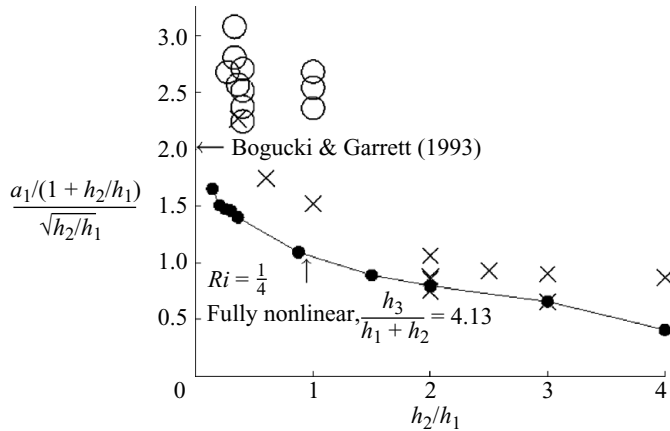


FIGURE 2. Present observations of breaking (\circ) and non-breaking (\times) compared to calculations of critical amplitude, assuming this occurs for $Ri = 1/4$: asymptotic result $a_c = 2\sqrt{h_2 h_1}$ (valid for $h_2/h_1 \rightarrow 0$, $a_1/h_1 \rightarrow 0$) and fully nonlinear computations with $h_3/(h_1 + h_2) = 4.13$ (solid line with symbols).

4. Experimental results and discussion

4.1. Stable waves

Experiments including stable, non-breaking waves, labelled by runs 12–24 in the lower part of table 1, are organized according to pycnocline thickness relative to the upper mixed-layer depth, increasing from $h_2/h_1 = 0.36$ in run 12 to $h_2/h_1 = 3.67$ in run 24, corresponding to comparatively thin and thick pycnoclines, respectively. The non-dimensional amplitude of the stable waves, except run 24, is in the range $a_1/(h_1 + h_2) \sim 1.06 - 1.56$. In run 24, this is $a_1/(h_1 + h_2) = 1.74$.

All stable (and breaking) waves have amplitudes larger than the critical amplitude corresponding to an amplitude of a wave with $Ri_{min} = 1/4$. This is visualized by fully nonlinear computations with $h_3/(h_1 + h_2) = 4.13$, varying h_2/h_1 , shown in figure 2. (These computations have been published earlier in Fructus & Grue (2004, figure 13b in their work) and Grue (2005, figure 14 in his work). Note that a few of the experimental amplitudes in runs with $h_3/(h_1 + h_2)$ less than 4.13 and $Ri < 1/4$ (see table 1) appear on the borderline of the computation with $h_3/(h_1 + h_2) = 4.13$.

The figure also indicates the critical amplitude of $a_c = 2\sqrt{h_1 h_2}$, which is an asymptotic result, valid for $h_2/h_1 \rightarrow 0$, $a_1/h_1 \rightarrow 0$, derived by Bogucki & Garrett (1993), who worked with long internal KdV and BO solitons moving along very thin pycnoclines and assumed that breaking occurs for $Ri_{min} = 1/4$. By use of a factor of $1 + h_2/h_1$ (found by trial and error), it is seen here that all breaking waves occur for amplitudes above a threshold of $a_1 = 2.24\sqrt{h_1 h_2}(1 + h_2/h_1)$, $h_2/h_1 < 1$. The stable waves all have amplitudes below this threshold. The highest stable wave moving along a thin pycnocline with $h_2/h_1 = 0.36$ has amplitude corresponding to that threshold, while waves moving along comparatively thicker pycnoclines have amplitudes that are far below.

The symmetrical behaviour (along the propagation direction) of the non-breaking waves with moderate to thick pycnoclines is illustrated in figure 3(a–c) by three of the stable runs, 13, 18 and 24, with pycnocline thicknesses of $h_2/h_1 = 0.36$, 2 and 4 and non-dimensional amplitudes of $a_1/(h_1 + h_2) = 1.36$, 1.21 and 1.74, respectively. Note that the leading edge of the wave appears at the left of the figures and the tail

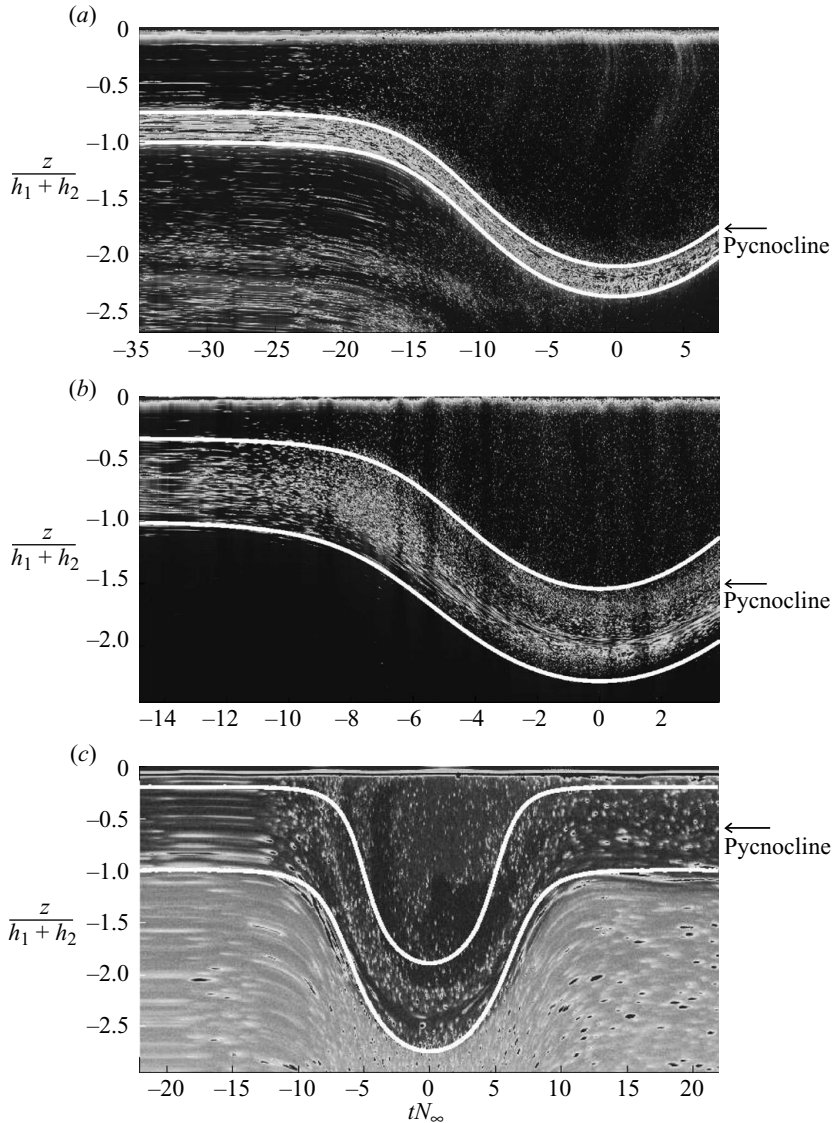


FIGURE 3. For legend see next page.

to the right, since these plots are in the time frame. There is higher concentration of particles within the pycnocline, and thus higher reflectivity, than in the upper and lower layers. The pycnocline is indicated in the plots. From the measured velocity field, the experimental stream function is obtained by integration, without smoothing, and compared to computation, for all waves, with good comparison. An example is shown in figure 4.

Measurement and theoretical computation of the velocity field of strong non-breaking waves exhibit a horizontal velocity in the upper layer up to 0.9 times the nonlinear wave phase velocity and down to -0.8 times c in the lower layer (run 24; see figure 5 and in particular 5d). The experimental velocity profile extracted from a few velocity vector columns at the crest exhibits a good match to computation all along

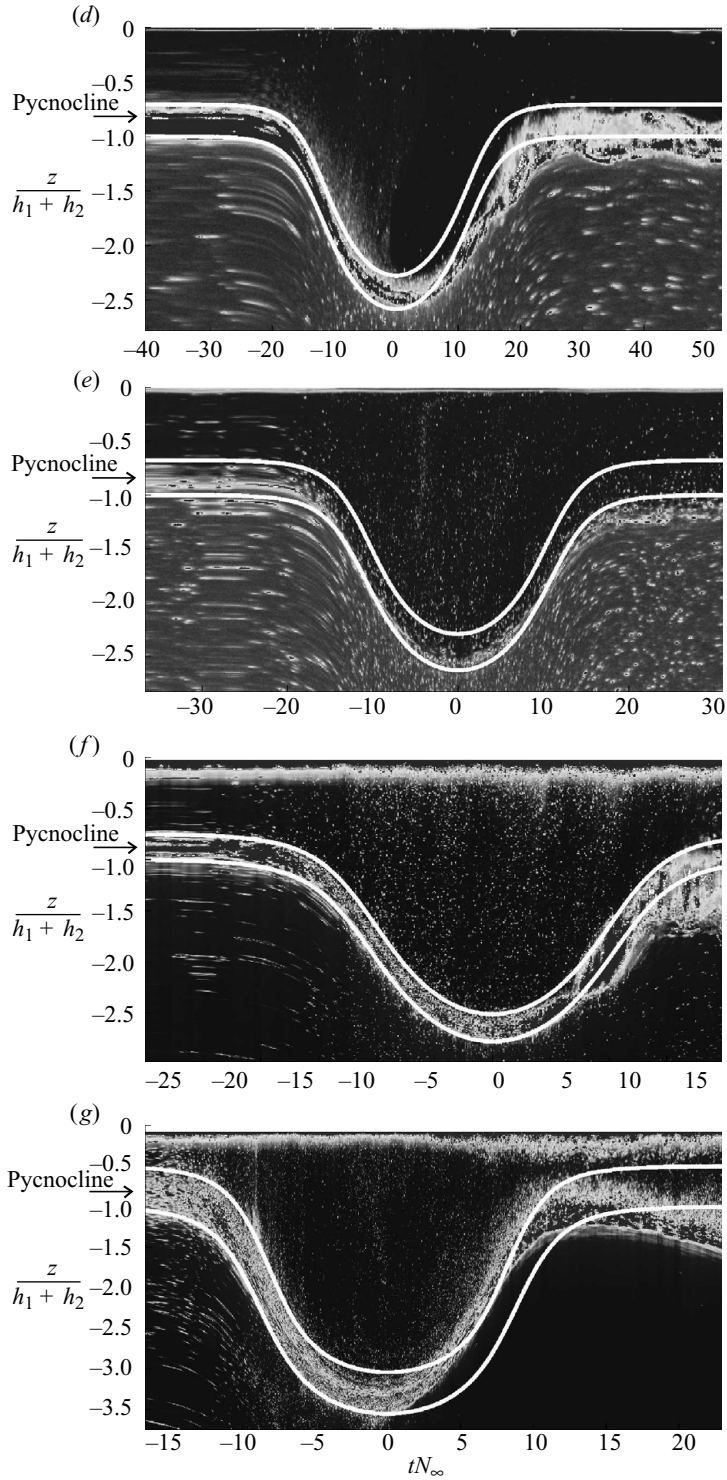


FIGURE 3. Stable and breaking waves. Leading part of wave to the left in plots. Stable runs (a) 13, (b) 18, (c) 24; breaking runs (d) 1, (e) 2, (f) 8, (g) 11.

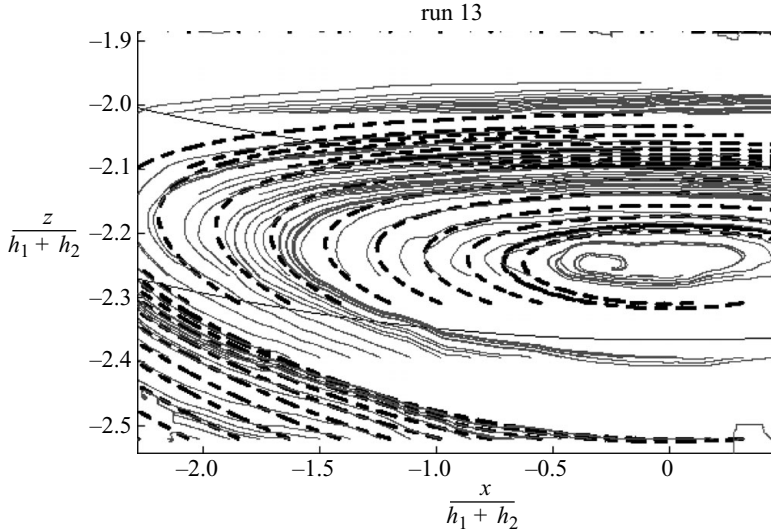


FIGURE 4. Experimental (thin solid line) and computational (thick dashed line) streamfunction in run 13.

the vertical. Note some minor deviations in the very upper part of the pycnocline in run 24 and in the very lower part of the upper layer and also somewhat larger deviations in experimental $u(z)$ at wave maximum in the very upper part of the upper layer. The figure confirms that the velocity tends to zero at the upper boundary. The computed Richardson number can be seen in figure 6. In run 24, $Ri(z)$ becomes almost antisymmetric across the thick pycnocline (figure 6d). For reference, the values of minimum Richardson number computed for some of the stable cases are $Ri_{min} = 0.13$ (run 20), $Ri_{min} = 0.12$ (runs 12, 13), $Ri_{min} = 0.11$ (run 20) and $Ri_{min} = 0.087$ (run 24).

4.2. Experiments that exhibit breaking

Eleven of the runs exhibited breaking. Results are summarized in the upper part of table 1, with runs labelled with numbers from 1 to 11. The pycnocline thickness is in the range $h_2/h_1 \sim 0.27 - 1$ and non-dimensional amplitude in the range $a_1/(h_1 + h_2) \sim 1.39 - 2.54$. All of the breaking waves have

$$a_1 > 2.24\sqrt{h_1 h_2}(1 + h_2/h_1), \quad h_2/h_1 < 1$$

(see figure 2). The weakest amongst the breaking waves have a non-dimensional amplitude of $a_1/\sqrt{h_1 h_2}/(1 + h_2/h_1)$ of 2.24 (run 3, with $h_2/h_1 = 0.4$, $h_3/(h_1 + h_2) = 4.14$, $Ri_{min} = 0.105$) and of 2.36 (run 9, with $h_2/h_1 = 1$, $h_3/(h_1 + h_2) = 7$, $Ri_{min} = 0.096$). The strongest non-breaking wave has $a_1/\sqrt{h_1 h_2}/(1 + h_2/h_1) = 2.25$ (run 13, with $h_2/h_1 = 0.36$, $h_3/(h_1 + h_2) = 4.07$, $Ri_{min} = 0.12$). This indicates a breaking threshold based on amplitude, valid for h_2/h_1 up to 1.

Four of the waves are visualized in figure 3(d–g), showing traces of the computed interfaces as well as images from experiment. Note that there is high reflectivity within the pycnocline in which the density stratification tends to concentrate the neutrally buoyant particles at their equilibrium level. The breaking waves are characterized by the following behaviour:

(a) The leading part of all waves (to the left of the trough in figure 3) propagating along an initially linearly stratified pycnocline separating two homogeneous layers is

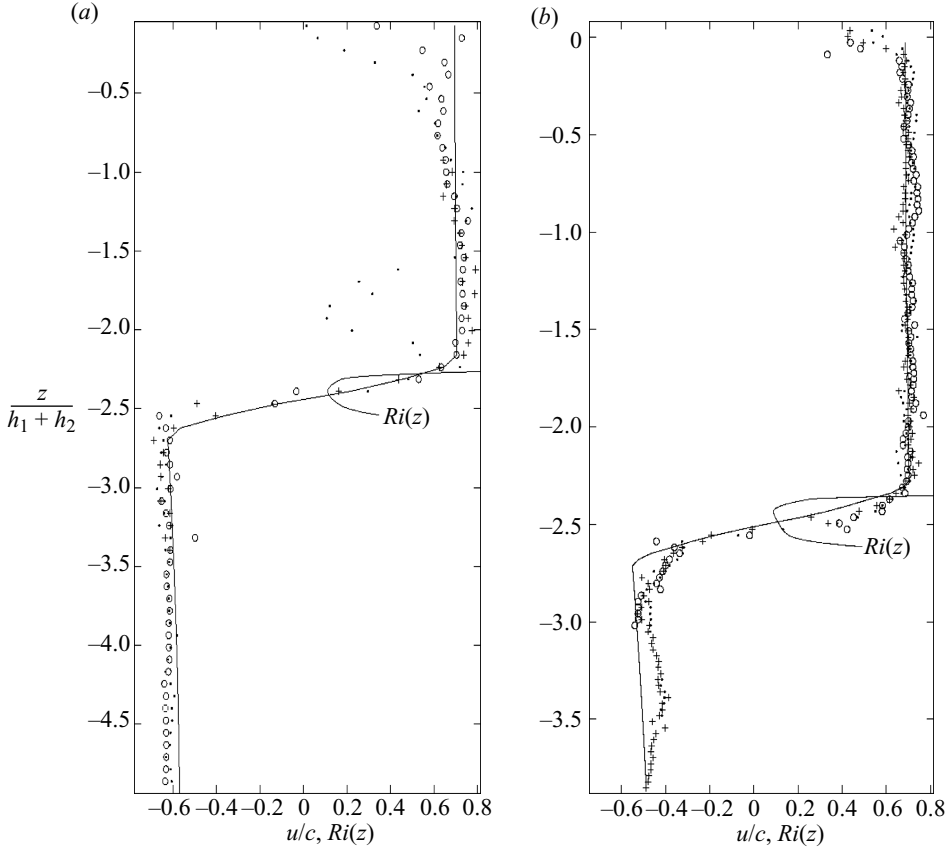


FIGURE 5. For legend see next page.

always stable. The characteristics of the leading part of the experimental waves are in agreement with predictions from computation assuming an idealized, steady wave.

(b) Instability develops at the maximum negative depression of the wave (i.e. at the trough).

(c) Notable differences in the tail of the experimental wave are shown when comparing experiment and computation. The measured motion within the pycnocline is seen to develop roll-like features that distort the homogeneous layers (see figure 7a). The initially organized rolls lead subsequently to turbulent motion within the pycnocline and eventual dissipation of the motion on small length scales.

The 11 runs with breaking waves may be divided into four subsets according to depth ratios between the layers at rest.

4.2.1. Subset one; pycnocline thickness 40% of upper-layer depth

Runs 1–4 were performed with depth ratios $h_2/h_1 = 0.4$, $h_3/(h_1 + h_2) \sim 4.14 - 4.29$ and non-dimensional wave amplitudes $a_1/(h_1 + h_2) \sim 1.42 - 1.71$. The experimental stream function in the leading part of the wave and up to about the crest (results not shown), as well as the velocity profile at wave maximum, compares well with computed values. Experimental velocities are obtained from three neighbouring velocity columns extracted from PIV (figure 5). (The velocity tends to zero at the upper fixed boundary at which the non-slip condition applies.)

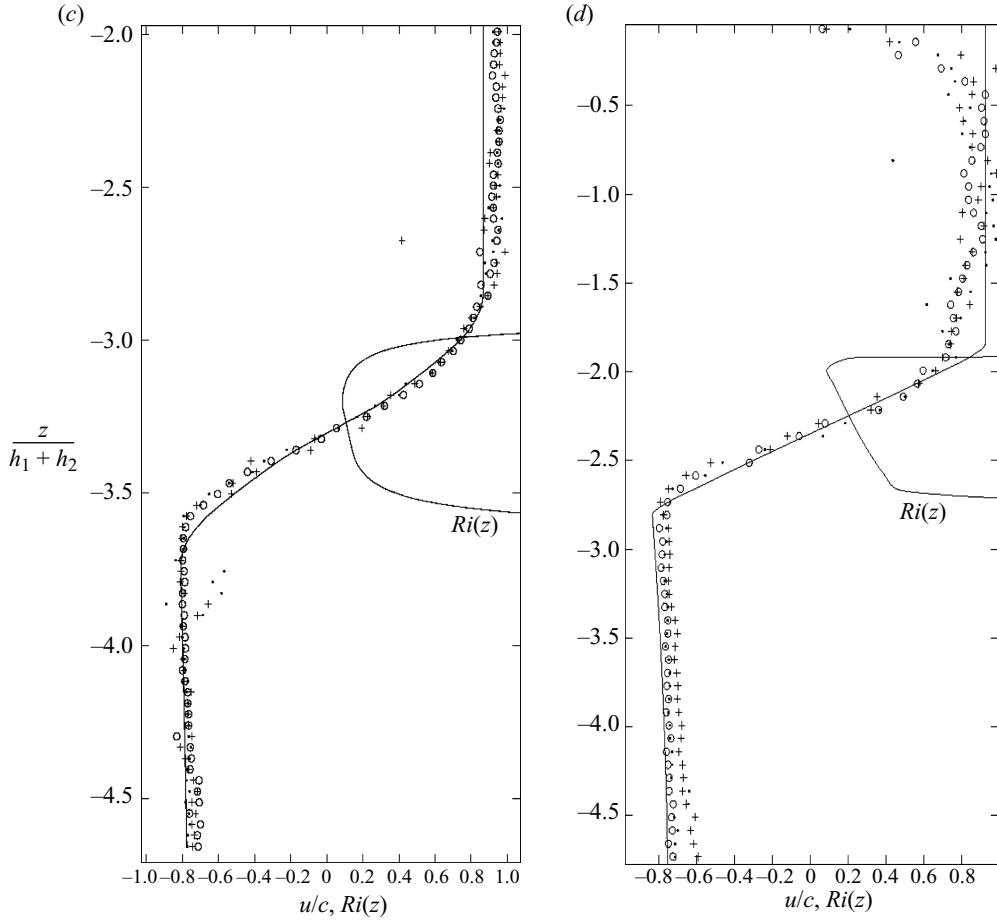


FIGURE 5. Experimental (symbols: \circ , $+$ and dots mark vectors from three neighbouring velocity columns) and computational (solid line) velocity profiles $u(z)/c$ and computational $Ri(z)$ (solid line, marked with $Ri(z)$) at wave maximum. (a) run 1; (b) run 8; (c) run 11, (d) run 24.

Computation of the Richardson number as a function of the vertical coordinate throughout the pycnocline is included in the velocity profile plots (see also figure 6). The computations show that Ri has a minimum of 0.112 at $z/(h_1 + h_2) \simeq -2.39$, corresponding to a level of about 40% from the top and 60% from the bottom boundary of the pycnocline, relative to its local thickness (run 1). The minimum is not very ‘peaky’, in the sense that Ri has a value in the range 0.112–0.12 in a rather significant fraction of the pycnocline. Similar computations of $Ri(z)$ are performed for the three other experiments in the subset, giving $Ri_{min} = 0.103$ in run 2, $Ri_{min} = 0.105$ in run 3 and $Ri_{min} = 0.10$ in run 4.

4.2.2. Subset two; effect of reducing the relative pycnocline thickness

In run 5 the pycnocline thickness is reduced from 40% to 36% of the upper-layer depth, but non-dimensional parameters are otherwise the same as in run 4. The thinner pycnocline enhances the shear, causing a slight reduction of the minimum Richardson number. In run 6, the pycnocline thickness is further reduced to 27% of

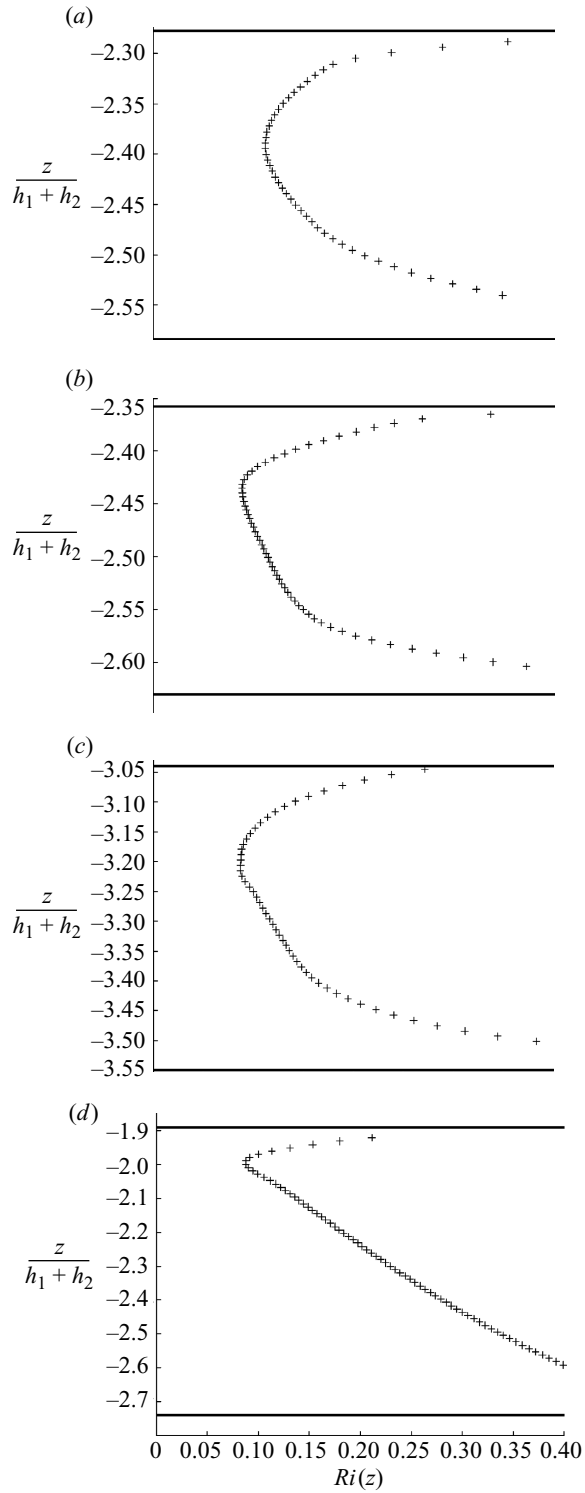


FIGURE 6. Computed Richardson number through the pycnocline. (a) run 1; (b) run 8; (c) run 11; (d) run 24.

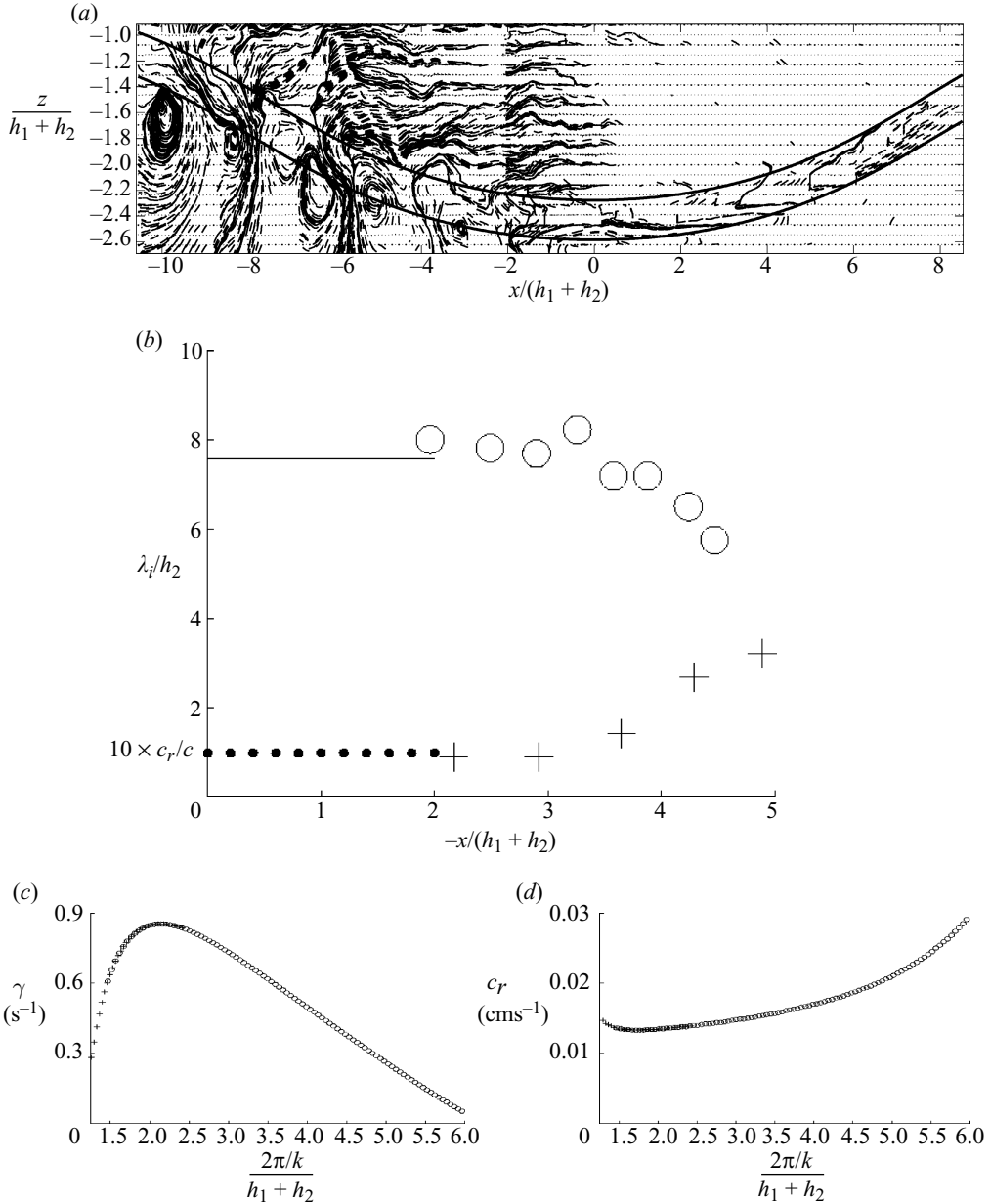


FIGURE 7. (a) Run 1. Stream lines corresponding to the difference in velocity fields between the numerical steady solution and experimental results. Only stream lines in the region in which the relative difference is larger than 10 % are drawn. (b) Observed wavelength (\circ) and propagation speed (+) of unstable modes versus distance from the trough. Wavelength of most unstable mode (solid) and propagation speed (dots) of the most unstable mode, calculated from solving the T-G equation. (c) Stability analysis (regular (+) and non-uniform (\circ) grids), results for growth rate $\gamma = kc_i$; (d) c_r versus relative wavelength $2\pi/k/h_1 + h_2$.

the upper-layer depth, causing a reduction of the minimum Richardson number in the experiment down to 0.08, even though the non-dimensional amplitude is smaller in run 6 than in run 5.

4.2.3. Subset three; effect of increasing $h_3/(h_1 + h_2)$

Runs 7 and 8 have pycnocline thickness $h_2/h_1 = 0.33$ and a deeper lower layer of $h_3/(h_1 + h_2) = 5.33$. Non-dimensional amplitudes are 1.61 and 1.76 respectively. Experimental and computational velocity profiles of run 8 show good agreement (figure 5*b*). The computational profile of $Ri(z)$ through the pycnocline is included in the figure, with an expanded version in figure 6(*b*). The minimum value of Ri in run 8 occurs about 25 % from the top of the pycnocline. As a function of the vertical coordinate Ri is more peaky in run 8 than run 1.

4.2.4. Subset four; pycnocline and upper layer equally thick

Subset three includes three breaking runs, 9–11. The pycnocline and upper layer are now equally thick, with lower-layer depth $h_3/(h_1 + h_2)$ in the range 6.7–7.25. Non-dimensional amplitudes of $a_1/(h_1 + h_2) = 2.36, 2.68, 2.54$ are 60–70 % higher in these runs compared to that of the previous ones. The experimentally determined and computed values of the streamlines and velocity profile at wave maximum show good agreement, with particularly good agreement in the top part of the pycnocline, where the profile of the Richardson number also has its minimum, as visualized for the strongest case of run 11 (figure 5*c*). The computational and experimental values of Ri_{min} are therefore very close. The minimum value of the Richardson number extends to about 10 % of the pycnocline thickness along the vertical and attains a value of 0.096 in run 9, 0.087 in run 10 and 0.086 in run 11.

4.3. Observation of KH billows and stability calculations

Figure 7(*a*) shows synoptically the deviation of the streamlines of the experimental velocity field from the steady (computational) wave in run 1. The plot shows clearly that the magnitude of this deviation is greater downstream of the trough (left side of the frame) than upstream. The billowing formed at the trough of the wave is a result of KH instability and manifests in the plot as a series of clockwise-rotating, discrete eddy features. By tracing the positions of the billows as they advect downstream during the wave evolution, their centre-to-centre wavelength may be estimated as a function of distance from the trough. The propagation speed may also be extracted from the data. The results presented in figure 7 show that, close to the wave maximum, the billows have a wavelength of $\lambda_i = 7.9h_2$ and speed of $c_r = 0.09c$. The billows have a tendency to shorten in the downstream flow, while the speed increases with distance.

The propagation speed and growth rate of the most unstable modes observed in experiment may be calculated from a stability analysis solving the T-G equation (see (1.1) in Hazel 1972). As input to the stability calculations performed here the computational velocity profile and Brunt–Väisälä frequency of each experiment, at wave maximum, are used. See, for example, the velocity profiles $u(z)$ in figure 5 and $Ri(z)$ profiles in figure 6, the latter providing the Brunt–Väisälä frequency through the pycnocline. In the computations, it was assumed that the pycnocline depth relative to the wave width is very thin, i.e. $h_2/\lambda \ll 1$, where λ is the wave width. For example for run 1, $h_2/\lambda = 0.028$. A more general stability analysis valid for h_2/λ , not necessarily small and accounting for the horizontal variation of the velocity and density fields, is left for future study.

Integration of the stability equation yields the complex propagation speed of the disturbance $c = c_r \pm i|c_i|$ (c_r propagation speed and $k|c_i|$ growth rate of perturbation) given the wavenumber k , where the latter is continuous. Numerical integration using regular and non-uniform grids (1760 and 440 collocation points, giving same result) provides $c_r(k)$ and $k|c_i(k)|$ (see figure 7*c,d*). From each computation the wavenumber

with maximal growth rate $\gamma = k|c_i(k)_{max}|$ and corresponding propagation speed c_r are identified. For run 1, the most unstable mode has $\lambda_i = 7.6h_2$ and speed $c_r = 0.09c$, with good agreement to the observation in experiment. We note that the stability analysis described exhibits a computational billow wavelength of $\lambda_i/h_2 = 7.5 \pm 0.7$ for all the runs with breaking waves. The growth rate is stronger for the waves that break than for those which are stable (see table 1 and § 5.1).

4.4. Comparison to field measurements of breaking ISWs

The present measurements may be compared to field measurements of breaking ISWs propagating shoreward on Oregon's continental shelf. The Richardson number estimated from observation was larger than $1/4$ (Moum *et al.* 2003). One of the waves that was observed to break had a rather thin pycnocline, with level at rest at depth $h_1+h_2 = 12$ m and amplitude $a_1 = 20$ m (Moum 2007, personal communication). Hence $a_1/(h_1+h_2) = 1.67$ in the observation, corresponding to an amplitude that is an average of runs 1–8. The velocity profiles in figure 5(a, b) illustrate the corresponding velocity profile of the wave in field observation. From the results in table 1, it is possible to infer that $Ri_{min} = 0.10 \pm 0.013$ and the length of the KH rolls is $\lambda_i = 7.6h_2$, the latter corresponding to 24 m in the field.

4.5. Comparison to observations of breaking periodic internal waves

Planar-laser-induced fluorescence visualization by Troy & Koseff (2005) of the motion within a 1 cm thin pycnocline sandwiched between two equally thick homogeneous layers, driven by periodic interfacial mode-1 waves of large amplitude showed that the breaking mechanism they observed was a modified shear instability, with characteristic KH billow roll-up and collapse. The KH instability originated at the high-shear wave crest and trough regions. The rolls in our experiments are about 80 % longer than those observed experimentally by Troy & Koseff (2005), indicating different velocity and density profiles in the two different experiments. The billow lengths obtained by Troy & Koseff (2005) in their inviscid calculations were about half of their experimental observations and may be due to the velocity shear and density variation across the pycnocline being rather different in their experimental and theoretical models. They did not measure the velocity profile within the pycnocline, nor did they calculate the actual nonlinear velocity profile in their theoretical estimate. Their estimation of a breaking threshold consistent with a minimum Richardson number in the range $Ri_w \sim (0.07 - 0.08) \pm 0.03$ may be questioned, since the estimate is based upon the use of theoretical velocity and density profiles that are not validated in their experiment. The experiments presented here show breaking at $Ri_{min} = 0.11$ (run 1) and a non-breaking wave with an even smaller Ri_{min} of 0.087 (run 24), for example.

Troy & Koseff (2005, figure 8 in their work) determined a wavenumber-dependent onset of breaking and concluded that breaking occurred when $ka \simeq \sqrt{2kh_2}$, where k is the wavenumber (cf. figure 8a). The measurements of breaking presented here fall within the range $0.1 < 2\pi h_2/\lambda < 0.25$ and have somewhat larger non-dimensional amplitude (figure 8b). Although wave amplitude and wavelength for a progressive wavetrain and a solitary wave are defined differently ($a_1/2$ may be preferred as amplitude, since a_1 (or a_2) in this comparison is, indeed, the wave height of the solitary wave), observations of breaking occur for similar non-dimensional parameters here.

In a complementary study, Fringer & Street (2003) used a LES code with a stratification and physical dimensions similar to those of Troy & Koseff (2005). Periodic finite-amplitude internal waves broke as a result of an initial two-dimensional

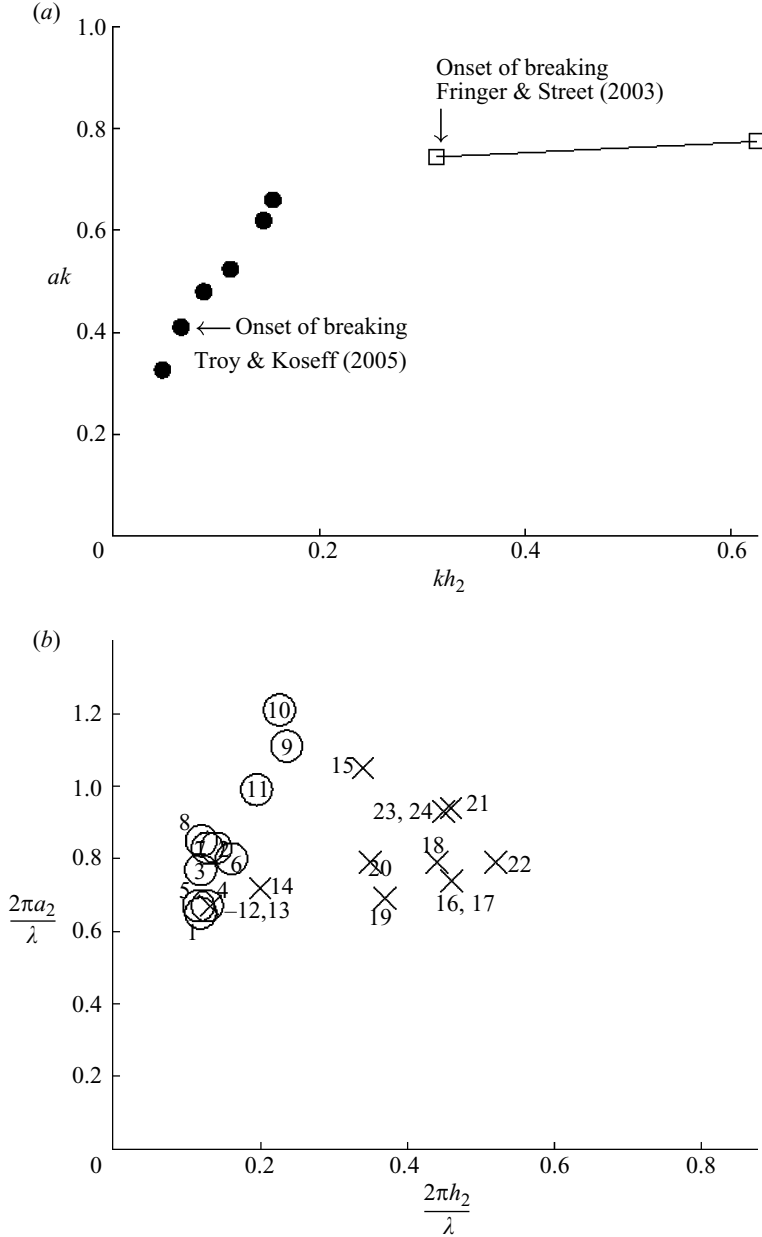


FIGURE 8. (a) Onset of breaking in periodic internal waves of amplitude a , wavenumber k and pycncline thickness h_2 , observed experimentally (Troy & Koseff, 2005) and numerically (Fringer & Street, 2003). (b) Present observations of breaking (○) and nonbreaking (×) solitary waves of amplitude a , wavelength λ (at half-amplitude), moving along a pycncline of thickness h_2 .

instability that led to a three-dimensional convective instability. The instability was divided into three regimes. In the first ($kh_2 < 0.56$), relevant to the present experiments, the most unstable wavelength was associated with a two-dimensional shear instability small enough to develop KH billows at the interface but not energetic enough to induce convective instability within the wave. For $kh_2 > 0.56$, waves with energetic

KH billows induced a convective instability. The critical Richardson number during breaking of $Ri_{min} = 0.13$ was evaluated directly from the vertical gradients of the density and velocity in computation, and the two first points of the threshold investigated by Fringer & Street (2003, figure 10 in their work) are included in figure 8a. A third regime concerns the range $kh_2 > 2.33$ and is outside the range of interest here.

5. The domain of $Ri < 1/4$

KH-like billows are a characteristic feature of the experimentally observed breaking waves. They are not present in the smaller non-breaking waves in which the shear is weaker. The observable billows in the motion when the wave amplitude and shear increase beyond certain levels indicate that the destabilizing effect of an unstable velocity profile dominates the stabilizing effect of the density profile. The inverse ratio between these effects is expressed in terms of the Richardson number. The velocity shear of the wave takes place over a much longer horizontal extent than the width of the pycnocline (in run 1, $h_2/\lambda = 0.02$) and is a slowly varying function of time, when observed at a fixed position along the wave tank. The pycnocline away from the wave maximum is slightly tilted (in run 1, $a_1/\lambda = 0.1$). For (breaking along) thinner pycnoclines the values of h_2/λ and a_1/λ are even smaller, but the motion within the pycnocline is then difficult to measure experimentally and obtain computationally. The partial use here of stability results for plane shear flow can mathematically be justified in the asymptotic limit when $h_2/\lambda \rightarrow 0$ and $a_1/\lambda \rightarrow 0$.

Differing from a parallel shear flow, the wave motion studied here obtains its minimum Richardson number at a single point, with all surrounding values of Ri being larger (including along the horizontal direction). A pocket of the wave of limited horizontal extent where Ri becomes less than a certain value, and where potentially unstable motion has the chance to grow ($Ri < 1/4$), is helpful in explaining the unstable motion that is observed in experiment.

In all present experiments, the minimum Richardson number is less than $1/4$, and the solitary wave has a small region (a ‘pocket’) of finite lateral extent in which Ri everywhere is less than $1/4$. Computations of the pocket with $Ri < 1/4$, which is a pocket of possible linear instability, are obtained for all experimental waves, and indicated for run 18 in figure 9 (note the highly exaggerated vertical scale). The horizontal length of the pocket is denoted by L_x , a quantity that grows according to $L_x = \alpha_0(1 - 4Ri_{min})$ or, alternatively, $Ri_{min} = -L_x/(4\alpha_0) + 1/4$, where α_0 is a constant and $1/4 - Ri_{min}$ is a small, positive quantity. A horizontal length scale that is available as a reference length is the wave width, λ , of the ISW, defined as the width of the lower separation line of the pycnocline, at level of half-amplitude, $a_2/2$ (figure 9). The wave width, λ , is a highly nonlinear function of wave amplitude. Nonlinear computations of the wave width given in many works (Michallet & Bartélemy 1998; Stanton & Ostrovsky 1998; Ostrovsky & Grue 2003; Fructus & Grue 2004; Grue 2005) show that λ increases with increasing $a_1/(h_1 + h_2)$ when this is larger than (about) 0.8 and decreases with increasing h_2/h_1 in this amplitude range. The computations by Ostrovsky & Grue (2003), compared to the COPE field measurements, show that λ decreases with increasing $h_3/(h_1 + h_2)$. The behaviour occurs for an amplitude range away from saturation and conjugate flow limit.

Plots of the experimental runs in the $(L_x/\lambda, Ri_{min})$ -plane show that all waves observed are in the range $Ri_{min} = -0.23L_x/\lambda + 0.298 \pm 0.016$ (figure 10). By close inspection, it is observed that experiments in which h_2/h_1 is small are close to the

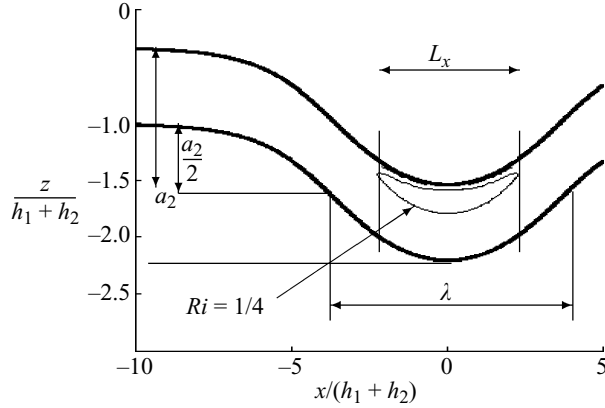


FIGURE 9. Computation of pocket of $Ri < 1/4$. Definition of horizontal length, L_x , of pocket of $Ri < 1/4$ and wave width, λ . Run 18.

upper boundary defined by $Ri_{min} = -0.23L_x/\lambda + 0.314$ (runs 1–5, 12–15). The same tendency is observed in cases in which the depth of the lower layer, $h_3/(h_1 + h_2)$, is somewhat reduced, as in runs 11 and 19. However, experiments with relatively thick pycnoclines, i.e. moderate to large values of h_2/h_1 , appear along the lower boundary, given by $Ri_{min} = -0.23L_x/\lambda + 0.282$ (runs 16–18, 20–24). Experiments with a thin pycnocline, but with increasing $h_3/(h_1 + h_2)$, are also close to the lower line in the plot; see particularly runs 6–10 of the breaking waves. Included in the plot is an observation of a breaking wave (induced by shear instability) from Grue *et al.* (1999, figure 7e in their work), where $Ri_{min} = 0.07$. The corresponding value of $L_x/\lambda = 1.03$ was recalculated here.

The plots in figure 10 indicate that the line

$$L_x/\lambda = 0.86$$

separates breaking and non-breaking waves and provides a breaking criterion for the present measurements. The separation line $L_x/\lambda = 0.86$ provides a sharper condition than a breaking criterion based on a minimum Richardson number.

The results indicate that L_x/λ provides a sufficient criterion for breaking. The interpretation is that breaking is observed when the potentially unstable modes of the core of the wave have sufficient time to grow. This time is proportional to the horizontal region of instability of the wave. The relevant reference length scale is the wave width (measured here at the vertical excursion of the pycnocline corresponding to the half amplitude, relative to rest). The weakest breaking waves all have a value of L_x/λ that is slightly above 0.86. The strongest non-breaking wave (run 24) has $L_x/\lambda = 0.86$ (and $Ri_{min} = 0.09$).

It is noted that the value of $Ri(z)$ and its minimum Ri_{min} is very sensitive to the width of the pycnocline (see figure 5, particularly 5d in the case of a thick pycnocline). The observations show that the minimum value of Ri is in the range between 0.09 and 0.11 for the weakest breaking waves illustrated in figure 10 and relative pycnocline width in the range $0.33 < h_2/h_1 < 1$. The value of Ri_{min} does not provide a good indication of breaking. Assessment of accuracy is further discussed in § 5.2.

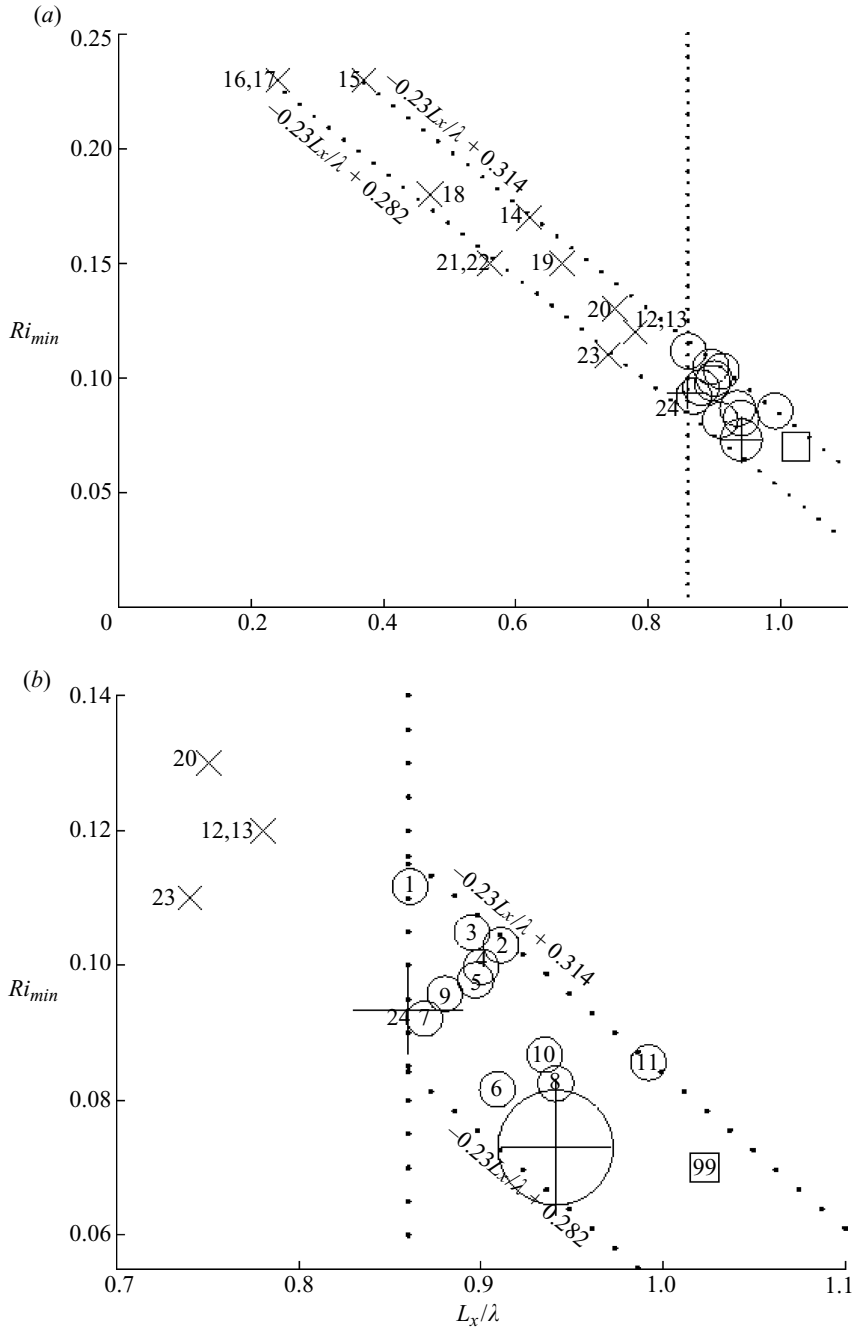


FIGURE 10. (a) All experiments and (b) close-up, plotted in the $(L_x/\lambda, Ri_{min})$ -plane. Stable waves runs 12–23 (\times) and run 24 ($+$). Waves with breaking, runs 1–11 (\circ), Grue *et al.* (1999; \square). Breaking run 8 is marked with $+$ and \circ combined, indicating $Ri_{min} = 0.073 \pm 0.01$. Range of results: $Ri_{min} = -0.23L_x/\lambda + 0.298 \pm 0.016$. Separation line between non-breaking and breaking waves at $L_x/\lambda = 0.86$.

5.1. Estimated growth of the computed instability

The unstable perturbations that grow in the region behind the trough undergo an amplification e^F , where F may be estimated by

$$F = t_{\text{growth}}\gamma,$$

where $\gamma = kc_i$ corresponds to the maximal growth rate obtained in the stability calculations introduced in §4.3 (see table 1). The time period the instability may grow can be estimated by $t_{\text{growth}} = \frac{1}{2}L_x/(c - c_r)$, where $c - c_r$ denotes the speed of the perturbation relative to the wave motion. For large values of F , unstable modes are expected to have sufficient time to grow to finite amplitude and thereby trigger wave breaking. Conversely, when F is small, unstable modes are not expected to grow sufficiently large before leaving the unstable region. Predictions from the stability analysis presented in table 1 show that, for thin pycnoclines with h_2/h_1 in the range 0.27–0.4, F exceeds 2.7 for the unstable runs 1–8, while $F = 1.5$ for the stable runs 12 and 13, also with thin pycnocline ($h_2/h_1 = 0.36$). Note particularly that all of the three weakest breaking runs 1, 2 and 7 have F in the range 2.7–2.8, giving a growth of the instabilities that becomes $e^{2.7-1.5} \simeq 3.3$ (or $e^{2.8-1.5} \simeq 3.7$) times larger than the stable runs 12 and 13. The growth rate of unstable modes decays for comparatively thicker pycnoclines, giving a value of $F = 1.9$ for run 9, the weakest breaking wave among the runs 9–11 with $h_2/h_1 = 1$. For comparison, the stable run 20, with $h_2/h_1 = 2$, has $F = 0.6$, meaning that the growth of an instability in run 9 is $e^{1.9-0.6} \simeq 3.7$ times larger than in run 20. For still wider pycnocline, the growth rate is still reduced. Note that value of non-dimensional growth rate $\gamma(h_1 + h_2)/c_0$ increases from 0.11 to 0.16, and F from 0.4 to 0.7, from stable run 23 to stable run 24.

5.2. Assessment of accuracy

Assessment of the similar runs 1–6 gives average values of Ri_{\min} and L_x/λ of 0.10 and 0.89, respectively, and standard deviations of 7% and 2%, respectively. These values are obtained for waves that have a relative variation in the amplitude of 10% and imply that breaking occurs when Ri_{\min} becomes lower than 0.10 and L_x/λ exceeds 0.89. For run 1 we note that experimental u/c , and the wavelength and propagation speed of the KH billows, are very close to those in the computation and stability analysis, respectively, giving another indication of the accuracy of the results (in run 1). The velocity profiles shown in figure 5(a–d) may be used to judge the accuracy of estimating Ri_{\min} in the experimental runs: For run 8 we note that computational $1 - u/c \simeq 0.67$ while the experimental value $1 - u/c \simeq 0.53$ for $z/(h_1 + h_2) = -2.425$, where Ri has its minimum. Using formula (3.2) for the Richardson number, this reduces the estimate of Ri_{\min} from 0.083 in computation to 0.064 in experiment. The value of Ri_{\min} in run 8 is thus in the range 0.073 ± 0.01 . In run 11 experimental and computational u/c are very close.

Inspection of $1 - u/c$ in run 24 shows that computation gives $1 - u/c \simeq 0.321$, while experiment gives $1 - u/c = 0.367$ at vertical coordinate $z/(h_1 + h_2) = -2$, where Ri is the smallest. Using formula (3.2) for the Richardson number, the experimental estimate of Ri_{\min} becomes 0.10. We further note that the three runs 22, 23 and 24, all with experimental pycnoclines approximately 6 cm thick and similar mixed-upper-layer thicknesses, have non-dimensional amplitudes of $a_1/(h_1 + h_2) = 1.14, 1.56$ and 1.74 respectively. The values of Ri_{\min} are 0.15 and 0.11 (run 22 and run 23 respectively; see table 1). By linearly extrapolating the decrease of Ri_{\min} with increasing $a_1/(h_1 + h_2)$ we obtain $R_{\min} = 0.09$ in run 24, very close to the computational value of 0.087. We may conclude that Ri_{\min} is in the range 0.087 – 0.10 in run 24. The value of L_x/λ

(in run 24) may similarly be obtained by extrapolating the values of L_x/λ in the similar runs 22 and 23, giving $L_x/\lambda = 0.823$, very close to the computational estimate of 0.86.

5.3. Effect of the Reynolds number

A Reynolds number may be introduced by $Re = \Delta u h_2 / 4\nu$, following the usual definition for stratified shear flows, where h_2 is the pycnocline thickness, ν kinematic viscosity and Δu the velocity jump across the pycnocline. The stability of a stratified shear flow is known to be affected by viscosity for $Re \leq 100$ (Hogg & Ivey 2003), the effect being that viscosity reduces the growth rate and damps the high wavenumber perturbations, lowering the most unstable perturbation wavenumber. In the present experimental study, the Reynolds number ranges from approximately 800 in run 1 to 10 000 in run 20, being, therefore, one to two orders of magnitude larger than the maximum value at which viscosity is believed to affect dramatically the instability. It can be shown that scale effects are unimportant by comparing runs 4 and 5 which have (about) the same non-dimensional amplitude and depth ratios and similar behaviour of breaking, despite the fact that run 4 was in the smaller tank and run 5 in the larger, and the Reynolds number was about three times higher in run 5 than in run 4.

6. Summary and conclusion

The stability properties of 24 experimental ISWs of extremely large amplitude and minimum Richardson number (Ri) less than $1/4$, moving horizontally in a stratified fluid, have been investigated. A linearly stratified pycnocline of thickness h_2 was sandwiched between an upper homogeneous layer with thickness h_1 and a comparatively thicker lower homogeneous layer of thickness h_3 . PIV was used to measure wave-induced velocities, obtaining experimental stream functions, velocity profiles through the pycnocline (and elsewhere), wave speed, amplitude and, in cases of breaking, the stream function of the KH billows. Fully nonlinear computations of solitary wave motion in a three-layer fluid supported the measurements, obtaining: wave speed, amplitude (a_1), velocity field, streamlines, wave width λ and Ri . The lateral extent (L_x) and shape of the pocket in which $Ri < 1/4$ were computed.

The 11 ISWs that broke all had amplitudes in the range

$$a_1 > 2.24\sqrt{h_1 h_2}(1 + h_2/h_1), \quad h_2/h_1 < 1,$$

(where the inclusion of the factor $1 + h_2/h_1$ was found by trial and error), while the stable ISWs had amplitudes on or below this limit. The limit given above is a generalization of the asymptotic threshold amplitude of $2\sqrt{h_1 h_2}$ derived by Bogucki & Garrett (1993), assuming occurrence of breaking for $Ri = 1/4$ (see illustration in figure 2). For the present breaking ISWs, the pycnocline was in the range $0.27 < h_2/h_1 < 1$, and the lower layer depth was in the range $4.14 < h_3/(h_1 + h_2) < 7.14$. For the stable ISWs, the pycnocline was in the range $0.36 < h_2/h_1 < 3.67$ and the lower layer depth in the range $3.22 < h_3/(h_1 + h_2) < 7.25$. The amplitudes of the stable waves moving along relatively thick pycnoclines were far below the amplitude threshold indicated above.

In the breaking case, run 1, the KH billow length and propagation speed were observed to be $\lambda_i/h_2 = 7.9$ and $c_r/c = 0.09$ respectively. A quasi-steady stability analysis solving the T-G equation with the nonlinear velocity and density profiles at wave maximum as input was used to calculate the growth rate and travelling speed of the perturbation, as functions of the wavelength. The most unstable mode had a

wavelength of $\lambda_i/h_2 = 7.5 \pm 0.7$, for all breaking waves, comparing well to experimental observation. The stability analysis showed that $\lambda_i/h_2 = 7.5 \pm 0.7$ also for the stable waves, but growth rates were then significantly smaller. The estimated growth of the most unstable modes was found to be more than 3.3–3.7 times higher for the waves that broke, compared to the strongest non-breaking waves, for corresponding h_2/h_1 . The growth decayed with increasing h_2/h_1 .

The minimum Richardson number (Ri_{min}), horizontal length (L_x) of the pocket with wave-induced $Ri < 1/4$, a pocket of possible instability and wavelength (λ) were evaluated for all runs. All measurements fell within the range $Ri_{min} = -0.23L_x/\lambda + 0.298 \pm 0.016$ in the $(L_x/\lambda, Ri_{min})$ -plane. In this range, the breaking ISWs were found for

$$L_x/\lambda > 0.86,$$

while stable ISWs were found for $L_x/\lambda < 0.86$. The breaking threshold of $L_x/\lambda = 0.86$ is sharper than one based on a minimum Richardson number. The physical interpretation is that unstable modes need some time to grow before breaking is observed. Computations show that $Ri(z)$ becomes almost antisymmetric across relatively broad pycnoclines, with Ri_{min} occurring towards the top part of the pycnocline.

We thank four anonymous referees for constructive criticism. D. Fructus, J. Grue and A. Jensen are grateful for the support of the Research Council of Norway, through the Strategic University Programme, *Modelling of Currents and Waves for Sea Structures*, at the University of Oslo. Technical support at the University of Oslo was provided by Svein Vesterby and Arve Kvalheim. M. Carr and P. A. Davies are grateful for the support of a grant from the UK Engineering and Physical Sciences Research Council (EPSRC) under its Physics–Engineering Programme. Technical support at the University of Dundee was provided by John Anderson and Gary Conacher.

Appendix. Nonlinear three-layer motion by integral equations

In the case of nonlinear motion the field equation in the homogeneous top and bottom layers is the Laplace equation. In the midlayer with constant Brunt–Väisälä frequency (at rest) the field equation reads

$$\nabla^2 \psi_2 + \frac{N_\infty^2}{c^2} \psi_2 = 0, \quad (\text{A1})$$

where c denotes the nonlinear wave speed.

An interface I localized at $z = \eta(x) - h_1$ separates the upper layer number one from the midlayer number two. Likewise, an interface \hat{I} localized at $z = \hat{\eta}(x) - h_1 - h_2$ separates the midlayer number two from the lower layer number three. The values of η and $\hat{\eta}$ vanish for $x \rightarrow \pm\infty$. The wave motion is taking place between the rigid lids at the top and bottom boundaries of the fluid layer in which the boundary conditions are $\psi_1 = 0$ at $z = 0$ and $\psi_3 = 0$ at $z = -h_1 - h_2 - h_3$.

The kinematic and dynamic boundary conditions at the separation line at $z = \eta(x) - h_1$ gives that

$$\frac{\partial \psi_j}{\partial s} - c \frac{\partial \eta}{\partial s} = 0, \quad j = 1, 2, \quad (\text{A2})$$

$$\frac{\partial \psi_2}{\partial n} = \frac{\partial \psi_1}{\partial n}, \quad (\text{A3})$$

with both satisfied at I , where s denotes the arclength along I and n the normal, pointing out of midlayer 2. Similar relations hold for $\psi_{2,3}$ at the lower boundary \hat{I} with η replaced by $\hat{\eta}$.

The nonlinear wave problem is solved by means of integral equations. The relevant Green function satisfies the Helmholtz equation in each of the layers. For this purpose, we introduce the function

$$Z_0(\alpha, \hat{x}) = Y_0(\hat{x}) + \alpha J_0(\hat{x}), \quad (\text{A4})$$

where J_0 and Y_0 denote Bessel functions of order zero, of first and second kinds, respectively, and α a real constant to be chosen (Fructus & Grue 2004). The importance of the non-singular term $\alpha J_0(\hat{x})$ is indicated in (A12) below; $Z_0(\alpha, \hat{x})$ behaves like $\ln \hat{x}$ for $\hat{x} \rightarrow 0$. In the upper layer the choice of Green function reads $G_1(x, z, x', z') = \ln(r/r_1)$, where $r = [(x-x')^2 + (z-z')^2]^{1/2}$ and $r_1 = [(x-x')^2 + (z+z')^2]^{1/2}$; G_1 becomes zero at $z=0$. In the midlayer the function

$$G_2(x, z, x', z') = \frac{\pi}{2} Z_0(\alpha, rN_\infty/c) \quad (\text{A5})$$

is used, and in the lower layer, $G_3(x, z, x', z') = \ln(r/r_3)$, where $r_3 = [(x-x')^2 + (z+z'+2H)^2]^{1/2}$. The function G_3 becomes zero at $z = -H = -(h_1 + h_2 + h_3)$. The stream functions are determined by singularity distributions, i.e.

$$\psi_1 = \int_I \sigma_1(s') G_1(x, z, x'(s'), z'(s')) ds', \quad (\text{A6})$$

$$\psi_3 = \int_{\hat{I}} \sigma_3(s') G_3(x, z, x'(s'), z'(s')) ds', \quad (\text{A7})$$

$$\psi_2 = \int_I \sigma_2(s') G_2(x, z, x'(s'), z'(s')) ds' + \int_{\hat{I}} \hat{\sigma}_2(s') G_2(x, z, x'(s'), z'(s')) ds', \quad (\text{A8})$$

where $\sigma_1, \sigma_2, \hat{\sigma}_2, \sigma_3$ denote distributions to be determined. The kinematic boundary conditions (A2) give, at I ,

$$PV \int_I \sigma_1(s') \frac{\partial G_1}{\partial s} ds' - c \frac{\partial \eta}{\partial s} = 0, \quad (\text{A9})$$

$$PV \int_I \sigma_2(s') \frac{\partial G_2}{\partial s} ds' + \int_{\hat{I}} \hat{\sigma}_2(s') \frac{\partial G_2}{\partial s} ds' - c \frac{\partial \eta}{\partial s} = 0, \quad (\text{A10})$$

where PV means principal value. The condition (A3) gives

$$\pi[\sigma_1(s) + \sigma_2(s)] + \int_I \left(\sigma_2(s') \frac{\partial G_2}{\partial n} - \sigma_1(s') \frac{\partial G_1}{\partial n} \right) ds' + \int_{\hat{I}} \hat{\sigma}_2(s') \frac{\partial G_2}{\partial n} ds' = 0. \quad (\text{A11})$$

The integral equations ((A9)–(A11)) are complemented by a set of similar equations at the lower boundary \hat{I} . The six equations determine the four unknown singularity distributions $\sigma_1, \sigma_2, \hat{\sigma}_2, \sigma_3$ and the profiles η and $\hat{\eta}$. The computations are initiated by weakly nonlinear KdV solution, and small increments in the wave speed c are specified. The linear part of the integral equation operator is inverted analytically by means of Fourier transform, giving $\mathcal{A}(k)X(k) = \mathcal{F} \{ \mathcal{NL}(X) \} (k)$,

$$\mathbb{X} \begin{pmatrix} \mathcal{F} \{ \sigma_1 \} \\ \mathcal{F} \{ \sigma_2 \} \\ \mathcal{F} \{ \widehat{\sigma}_2 \} \\ \mathcal{F} \{ \sigma_3 \} \\ \mathcal{F} \{ \eta \} \\ \mathcal{F} \{ \widehat{\eta} \} \end{pmatrix} \mathcal{A}(k) = \begin{pmatrix} \widehat{a}[1 - e^{-2|k|h_1}] & 0 & 0 & 0 & ick & 0 \\ \pi[1 + e^{-2|k|h_1}] & \pi & \beta_3^{(2)} & 0 & 0 & 0 \\ 0 & \beta_1^{(2)} & \beta_2^{(2)} & 0 & ick & 0 \\ 0 & \beta_2^{(2)} & \beta_1^{(2)} & 0 & 0 & ick \\ 0 & \beta_3^{(2)} & \pi & \pi[1 + e^{-2|k|h_3}] & 0 & 0 \\ 0 & 0 & 0 & \widehat{a}[1 - e^{-2|k|h_3}] & 0 & ick \end{pmatrix},$$

where \mathcal{F} denotes Fourier transform and $\widehat{a} = i\pi \text{sign}(k)$. The coefficients $\beta_i^{(j)}$ and the nonlinear terms $\mathcal{NL}_i, i = 1, 6$ are given in Fructus & Grue (2004). The set of equations involves the transform of the derivative of the Green function and appears in the following way:

$$\mathcal{F} \left\{ \left[Y_1(K|u|) + \alpha J_1(K|u|) \right] \frac{u}{|u|} \right\} = \begin{cases} \frac{-2\alpha ik}{K\sqrt{K^2 - k^2}}, & |k| < K, \\ \frac{2ik}{k\sqrt{k^2 - K^2}}, & |k| > K, \end{cases} \quad (\text{A12})$$

where J_1 and Y_1 denote Bessel functions of order one, of first and second kinds, respectively, and $K = N_\infty/c$. The inclusion of the non-singular function, αJ_1 in the Green function means that the spectrum in Fourier space becomes complete.

REFERENCES

- ALEXAKIS, A. 2005 On Holmboe's instability for smooth shear and density profiles. *Phys. Fluids* **17**, 84–103.
- BOGUCKI, D. & GARRETT, C. 1993 A simple model for the shear-induced decay of an internal solitary wave. *J. Phys. Oceanogr.* **23**, 1767–1776.
- CARPENTER, J. R., LAWRENCE, G. A., & SMYTH, W. D. 2007 Evolution and mixing of asymmetric Holmboe instabilities. *J. Fluid Mech.* **582**, 103–132.
- CARR, M., FRUCTUS, D., GRUE, J., JENSEN, A. & DAVIES, P. A. 2008 Convectively-induced shear instability in large internal solitary waves. *Phys. Fluids* **20**, 12660.
- CAULFIELD, C. P. & PELTIER, W. R. 2000 Three dimensionalization of the stratified mixing layer. *Phys. Fluid* **413**, 1–47.
- DALZIEL, S. B. 2006 Digiflow user guide. <http://www.dampt.cam.ac.uk/lab/digiflow/>.
- DUDA, T. F., LYNCH, J. F., IRISH, J. D., BEARDSLEY, R. C. & RAMP, S. R. 2004 Internal tide and nonlinear wave behaviour in the continental slope in the northern South China Sea. *IEEE J. Ocean Engng* **29**, 1105–31.
- FRINGER, O. B. & STREET, R. L. 2003 The dynamics of breaking progressive interfacial waves. *J. Fluid Mech.* **494**, 319–353.
- FRUCTUS, D. & GRUE, J. 2004 Fully nonlinear solitary waves in a layered stratified fluid. *J. Fluid Mech.* **505**, 323–347.
- GARDNER, C. S., GREENE, J. M., KRUSKAL, M. D. & MUIRA, R. M. 1967 Method for solving the Korteweg–de Vries equation. *Phys. Rev. Lett.* **19**, 1095–1097.
- GRUE, J. 2005 Generation, propagation, and breaking of internal solitary waves. *Chaos* **15**, 037110–1–14.
- GRUE, J. 2006 Very large internal waves in the ocean – observations and nonlinear models. In *Waves in Geophysical Fluids – Tsunamis, Rogue Waves, Internal Waves and Internal Tides* (ed. J. Grue & K. Trulsen), pp. 205–270. Springer.
- GRUE, J., JENSEN, A., RUSÁS, P.-O. & SVEEN, J. K. 1999 Properties of large-amplitude internal waves. *J. Fluid Mech.* **380**, 257–278.
- HAZEL, P. 1972 Numerical studies of the stability of inviscid stratified shear flows. *J. Fluid Mech.* **51**, 39–61.
- HELFRICH, K. R. & MELVILLE, W. K. 2006 Long nonlinear internal waves. *Annu. Rev. Fluid Mech.* **38**, 395–425.

- HOGG, A. M. & IVEY, G. N. 2003 The Kelvin–Helmholtz to Holmboe instability transition in stratified exchange flows. *J. Fluid Mech.* **477**, 339–362.
- HOLMBOE, J. 1962 On the behaviour of symmetric waves in stratified shear layers. *Geophys. Publ.* **24**, 67–112.
- HOWARD, L. N. 1961 Note on a paper by John W. Miles. *J. Fluid Mech.* **10**, 509–512.
- KAO, T. W., PAN, F.-S. & RENUARD, D. 1985 Internal solitons on the pycnocline: generation, propagation, and shoaling and breaking over a slope. *J. Fluid Mech.* **159**:19–53.
- MICHALLET, H. & BARTÉLEMY 1998 Experimental study of interfacial solitary waves. *J. Fluid Mech.* **366**, 159–177.
- MILES, J. W. 1961 On the stability of heterogeneous shear flows. *J. Fluid Mech.* **10**, 496–508.
- MOUM, J. N., FARMER, D. M., SMYTH, W. D., ARMI, L. & VAGLE, S. 2003 Structure and generation of turbulence at interfaces strained by internal solitary waves propagating shoreward over the continental shelf. *J. Phys. Oceanogr.* **33**, 2093–2112.
- OSTROVSKY, L. A. & GRUE, J. 2003 Evolution equations for strongly nonlinear internal waves. *Phys. Fluids* **15** (10), 2934–2948.
- OSTROVSKY, L. A. & STEPANYANTS, Y. A. 2005 Internal solitons in laboratory experiments. *Chaos* **15**, 037111–1–28.
- PELTIER, W. R. & CAULFIELD, C. P. 2003 Mixing efficiency in stratified shear flows. *Annu. Rev. Fluid Mech.* **35**, 135–167.
- SCOTTI, R. S. & CORCOS, G. M. 1972 An experiment on the stability of small disturbances in a stratified free shear layer. *J. Fluid Mech.* **52**, 499–528.
- SMYTH, W. D., NASH, J. D. & MOUM, J. N. 2005 Differential diffusion in breaking Kelvin–Helmholtz billows. *J. Phys. Oceanogr.* **35**, 1004–1022.
- STANTON, T. P. & OSTROVSKY, L. A. 1998 Observations of highly nonlinear internal solitons over the continental shelf. *Geophys. Res. Lett.* **25** (14), 2695–2698.
- STAQUET, C. 2000 Mixing in a stably stratified shear layer: two- and three-dimensional numerical experiments. *Fluid Dyn. Res.* **27**, 367–404.
- SVEEN, J. K., GUO & GRUE, J. 2002 On the breaking of internal solitary waves at a ridge. *J. Fluid Mech.* **469**, 161–188.
- TROY, C. D. & KOSEFF, J. R. 2005 The instability and breaking of long internal waves. *J. Fluid Mech.* **543**, 107–136.
- TUNG, K.-K., CHAN, T. F. & KUBOTA, T. 1982 Large amplitude internal waves of permanent form. *Stud. Appl. Math.* **66**, 1–44.
- TURKINGTON, B., EYDELAND, A. & WANG, S. 1991 A computational method for solitary internal waves in a continuously stratified fluid. *Stud. Appl. Math.* **85**, 93–127.
- ZHU, D. Z. & LAWRENCE, G. A. 2001 Holmboe’s instability in exchange flows. *J. Fluid Mech.* **429**, 391–409.